

Article

Chemical Modification of Lherzolite Xenoliths Due to Interaction with Host Basanite Melt: Evidence from Tumusun Volcano, Baikal Rift Zone

Marina A. Gornova¹, Vasilii A. Belyaev¹ , Anas A. Karimov^{1,2,*} , Alexander B. Perepelov¹  and Sergei I. Dril¹

¹ Vinogradov Institute of Geochemistry, Siberian Branch of Russian Academy of Sciences, 1A, Favorsky St., 664033 Irkutsk, Russia

² Institute of the Earth's Crust, Siberian Branch of Russian Academy of Sciences, 128, Lermontova St., 664033 Irkutsk, Russia

* Correspondence: anas@igc.irk.ru; Tel.: +7-(914)0141927

Abstract: To investigate the process and chemistry of mineral reaction zone formation, we conducted detailed petrographic observations and chemical analysis of rocks and minerals of spinel lherzolite xenoliths from basanites of Tumusun volcano (Baikal Rift Zone). The reaction zones gradually disappear from contact toward the center of the xenoliths. The influence of basanite melt on major and trace element composition of secondary minerals of reaction zones is notable only at a distance up to 100–200 μm from the contact. At a distance of 0.3–1.0 mm from the contact, the major and trace composition of secondary clinopyroxenes from the orthopyroxene reaction zone indicates their formation from a melt formed by dissolution of orthopyroxene and influenced by the element diffusion from basanite melt. Inside xenoliths, the secondary minerals have Mg# values equal to or higher than Mg# of primary minerals, and secondary clinopyroxenes inherit their depleted or enriched REE pattern from primary pyroxenes. The compositional variations in secondary clinopyroxenes testify melt heterogeneity. Clinopyroxene rims have slightly higher LILE and similar abundances of other trace elements compared to clinopyroxene cores. This is consistent with the model developed from experimental studies: due to the interaction with basanite, incongruent dissolution of orthopyroxene occurs to form a melt which circulates in lherzolite and leads to pyroxenes and spinel dissolution. Diffusion of elements from basanite results in lherzolite enrichment in K, Na, Rb, Ba, La, and Ce, which are incorporated in feldspars and clinopyroxene of reaction zones as well as in feldspar veinlets. Non-dissolved mineral cores are homogenous and similar in major and trace element composition to primary minerals without reaction rims.

Keywords: mantle xenolith; lherzolite; clinopyroxene; basanite; reaction zone; melt-peridotite interaction; trace elements



Citation: Gornova, M.A.; Belyaev, V.A.; Karimov, A.A.; Perepelov, A.B.; Dril, S.I. Chemical Modification of Lherzolite Xenoliths Due to Interaction with Host Basanite Melt: Evidence from Tumusun Volcano, Baikal Rift Zone. *Minerals* **2023**, *13*, 403. <https://doi.org/10.3390/min13030403>

Academic Editor: Pei Ni

Received: 1 February 2023

Revised: 3 March 2023

Accepted: 9 March 2023

Published: 14 March 2023



Copyright: © 2023 by the authors. Licensee MDPI, Basel, Switzerland. This article is an open access article distributed under the terms and conditions of the Creative Commons Attribution (CC BY) license (<https://creativecommons.org/licenses/by/4.0/>).

1. Introduction

The studies of mantle peridotite xenoliths from alkaline basalts, kimberlites, and other mafic-ultramafic alkaline rocks allow reconstructing the processes operating in the Earth's mantle. These peridotites usually have reaction zones around their primary minerals. The mineral reaction zones apparently could be formed in the mantle and during transporting by host melts, or by both ways. Different models were suggested for the mineral reaction zone formation. At mantle conditions, the reaction zones could form as a result of metasomatic reactions [1,2], fluid- or melt-induced partial melting [3,4], or decompression-induced partial melting [5]. At crustal conditions, during transportation and ascend to the surface, the reaction zones are formed due to interaction of xenoliths with the host alkaline silica-undersaturated magmas [6,7] or decompression partial melting [8].

In discussions on the origin of reaction zones, the key arguments mainly include petrographic observations and compositions of secondary minerals and glass. In [8], the

textural and chemical (composition of associated glass) criteria were derived to differentiate between various possible origins of reaction zones in mantle clinopyroxene. The comparison of major element composition of primary clinopyroxene and secondary clinopyroxene from reaction zones of different origin does not allow distinguishing the reaction zones origin, since the pyroxenes exhibit similar compositional variations [8].

Apparently, the petrographic observations are the major point for distinction between mantle and crustal origin of mineral reaction zones. However, for petrographic observations, the size of xenoliths is important. In small xenoliths, all minerals could have reaction zones and it is sometimes difficult to establish preferential propagation of reaction zones relative to the host magma.

The previous studies of peridotite xenoliths from basanite of Miocene Tumusun volcano in Baikal Rift Zone found that the peridotites are fertile lherzolites exhibiting spongy clinopyroxene, feldspar-bearing pockets, and feldspar-rich veins [9,10]. The feldspar-bearing pockets are located next to resorbed grains of orthopyroxene and spinel and are composed of fine-grained aggregates of olivine, clinopyroxene, and feldspar. The feldspar has different composition: plagioclase occurs in spongy clinopyroxene and alkali feldspar occurs in the pockets. Initially, a genetic relation between feldspar-rich veins in the xenoliths and host basanite was suggested [9]. Later, the formation of spongy clinopyroxene as well as feldspar-bearing pockets and veins was interpreted as a result of mantle metasomatism induced by infiltration of alkali-rich and water-poor fluids [10]. The study of three large xenoliths available in our collection allowed us to establish a decrease in reaction zone development from basanite/xenolith contact toward center of xenoliths. Evidently, this suggests the formation of the mineral reaction zones in Tumusun lherzolite xenoliths as a result of peridotite–host magma interaction during xenoliths transportation up to the surface.

The occurrence of the reaction transformation of orthopyroxene of peridotite xenoliths at contacts with host alkaline basalts has been known for a long time (for example, [11]). Later, a series of experimental works was conducted and a two-stage interaction model for the formation of reaction zones in all peridotite minerals was developed [6,12,13]. In the first stage of this model, at the contact between xenolith and SiO₂-undersaturated alkaline melt the dissolution of orthopyroxene occurs to form silica- and alkali-rich melt and olivine and clinopyroxene. In the second stage, inside xenolith, a newly formed melt interacts with all peridotite minerals to form mineral reaction zones. The presence of alkali-rich glass and a high amount of clinopyroxene in orthopyroxene reaction zone is interpreted in terms of diffusion of alkalis and CaO from the host alkaline mafic melt into a newly formed melt. The Mg-rich composition of secondary olivine and clinopyroxene from reaction zones is interpreted as crystallization from a melt formed via pyroxenes dissolution [6].

The data on trace element behavior in the process of peridotite–host magma interaction are not abundant. In [7], the formation of reaction zones of all minerals from spinel lherzolite xenoliths in alkaline basalts of Deccan volcanic province is interpreted as a result of interaction with host alkaline basalts during xenolith transportation, as illustrated by petrographic observations, major element composition of secondary minerals, and distribution of Sr, REE, Zr, and Ti in the clinopyroxene core and spongy rim. In lherzolite xenoliths in leucitites of Morrón de Villamayor volcano (Calatrava volcanic field, Spain), the spongy clinopyroxene located at contact with the host leucitite rocks has higher trace-element (LILE, LREE, and HFSE) contents than primary clinopyroxene, suggesting a strong interaction with host melt during clinopyroxene recrystallization [14].

The information on possible changes in major and trace element composition of peridotite xenoliths due to their interaction with host SiO₂-undersaturated alkaline melts is essential, since such compositional changes should be considered for the correct interpretation of the mantle stage of xenolith formation.

In this paper, we present detailed petrographic observations and major and trace element geochemistry of peridotite xenoliths from Tumusun volcano. The data obtained were tested in terms of two-stage model of peridotite interaction with SiO₂-undersaturated

alkaline melt [6] and supply this model with the information on trace element behavior. The present study mainly aims to answer the question whether the mineral and whole-rock major- and trace-element composition can change or not in this interaction process.

2. Geological Position of Tumusun Volcano

The Baikal Rift Zone is a system of several sedimentation basins and axial and off-rift volcanic areas (Figure 1a). The Cenozoic basaltic volcanism of South Baikal volcanic area is active for 35 Ma from the Oligocene until the Holocene, and some researchers related this volcanism to the action of a mantle plume [15]. The largest volcanic impulse at 21–15 Ma formed a large lava plateau covered the Khamar-Daban Range [16,17]. The Cenozoic basaltic lavas erupted onto heterogeneous crustal basement made of metamorphosed fragments of island arc and back-arc complexes [18], which comprise metamorphic Khamar-Daman terrain. The Khamar-Daman terrain consists of several series: Slyudyanka (metamorphosed volcanogenic and sedimentary rocks), Khangarul (metamorphosed greywackes, tuffs and carbonates), and Khamardaban (metamorphosed flysch sediments). The accumulation of sediments occurred at 500–700 Ma [19], and high-grade metamorphism took place at 481–485 Ma [20]. The metamorphic rocks are extensively intruded by Paleozoic granitoids.

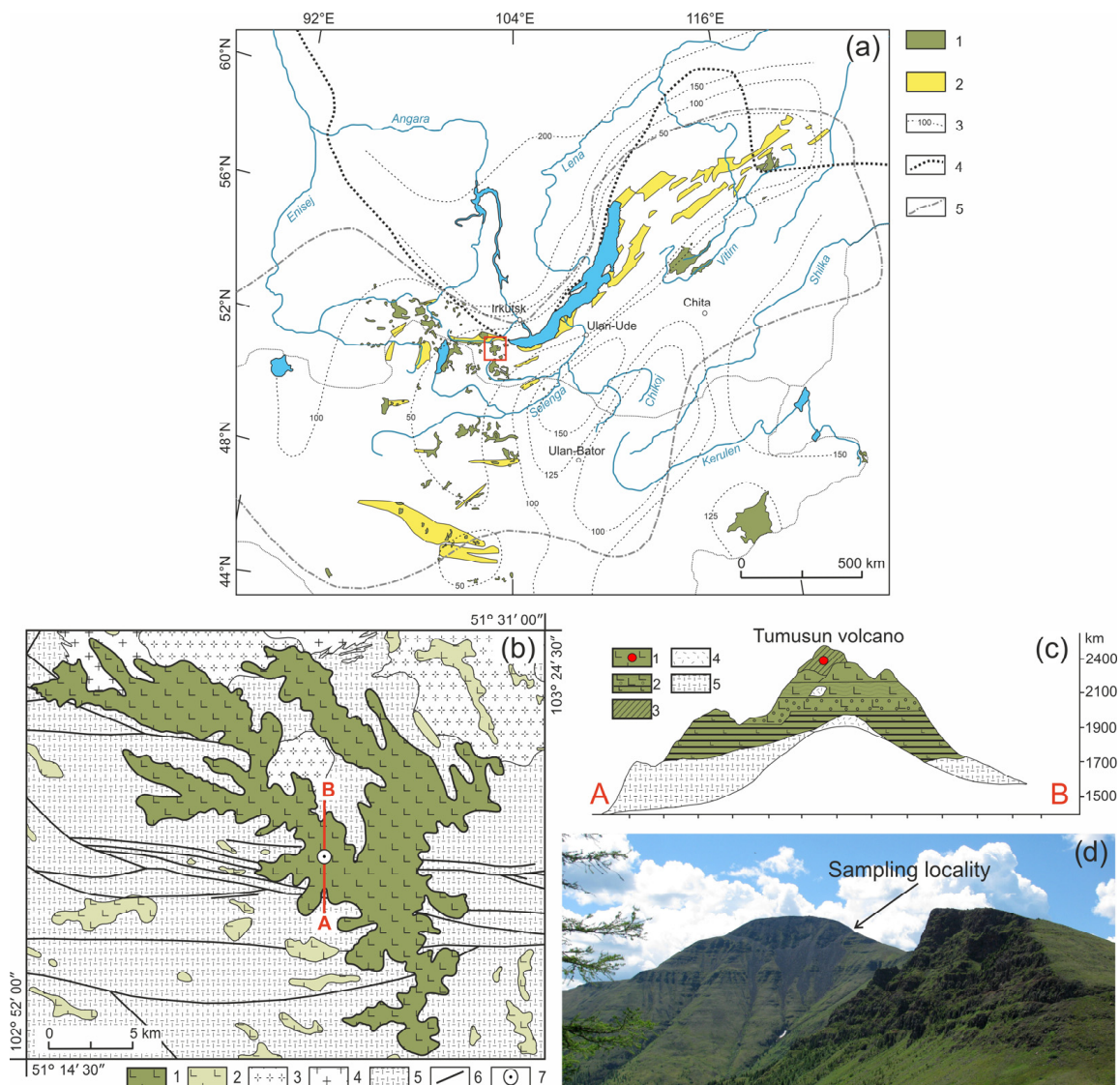


Figure 1. (a) Position of the Cenozoic volcanic areas in the Baikal Rift region [21]. 1—Cenozoic volcanic areas; 2—Cenozoic sedimentary basins; 3—lithosphere thickness (in km); 4—boundary of

the Siberian Craton; 5—boundary of distribution of anomalous mantle. The red square indicates the study area. (b) Geologic scheme of Tumusun area compiled by authors from State geological maps, sheets M48-I, M48-II, M48-VI, and M48-VII. 1–2—early-middle Miocene lavas of Tumusun plateau and other volcanic areas; 3—early Paleozoic granites and granodiorites; 4—late Proterozoic granites and granite gneisses; 5—metamorphic basement (gneisses and schists); 6—faults; 7—position of Tumusun volcano. The red line is location of cross-section shown in (c). (c) Cross-section of Tumusun volcano from [9]. 1—flood basalts; 2—interlayering of basaltic lavas, lava conglomerates and sands; 3—basaltic lava flows with xenolith material (marked by red circle); 4—relics of tefrite basalts; 5—metamorphic basement (gneisses and schists). (d) Landscape photograph of the Tumusun volcano with xenolith sampling locality.

The composition of lithospheric mantle beneath the Baikal Rift Zone and adjacent regions was studied by many authors [9,10,21,22]. One of the mantle xenolith localities is the Tumusun volcano (51°19′19″ N, 103°14′48″ E), which is located within the Khamar-Daman Range at watershed between the Tumusun and Utulik Rivers. The Tumusun volcano is one of the largest erupting centers among the other Neogene basaltic areas of the Khamar-Daban Range (Figure 1b). The thickness of Tumusun lava flows is up to 500 m. The rock types are alkaline olivine basalt, hawaiiite and, rarely, basanite. The volcanic sequence starts with voluminous eruptions of olivine basalt and hawaiiite, which comprise a major lava plateau, and ends with the formation of the Tumusun neck composed of basanite. The lavas of volcanic plateau were dated by the $^{40}\text{Ar}/^{39}\text{Ar}$ method at 16.9 ± 0.3 and 15.2 ± 0.2 Ma, and basanite of the Tumusun neck was dated at 12.6 ± 0.3 Ma [17]. Therefore, basanite magmas erupted on final stages of Tumusun volcano development. As shown for other regions of South Baikal volcanic area, the basanite melts erupt later and have a deeper source compared to that of hawaiiite melts [23]. The basanites of Tumusun volcano contain abundant mantle xenoliths of peridotite and pyroxenite. The xenolith-bearing basanite exhibits porphyric texture and contain phenocrysts of olivine (up to 0.6 mm in size) and subphenocrysts (0.2–0.3 mm) of olivine and subordinate clinopyroxene. Association of microlites includes olivine, clinopyroxene, plagioclase, and titanomagnetite. Interstitial space is made of nepheline, nepheline solid solutions, and anorthoclase. The major and trace element composition of xenolith-bearing basanite is listed in Electronic Supplementary Table S1. The peridotite xenoliths for present study were collected at slope of the Tumusun neck near the point with coordinates 51°19′22.90″ N, 103°14′40.70″ E. Among the studied collection, most of the xenoliths are small (with a size along three dimensions of 2–4–4–6–4–6 cm and one sample of only 1.5 cm in length), and only three are large (8–10–11–13–14–20 cm). At the contact between the xenolith and basanite, there are discrete reaction zones in the xenoliths.

3. Analytical Methods

The detailed petrographic observations were done with Olympus BX-51 optical microscope. The mineral identification was done with Tescan Mira 3 LMH scanning electron microscope (SEM) equipped with Oxford Ultim Max 40 energy-dispersive spectrometer (EDS). The mineral composition was acquired by electron probe micro analysis (EPMA) with JEOL JXA 8200 microprobe. Minerals were analyzed at accelerating voltage 20 kV, beam current 20 nA, probe diameter of 1 μm , and counting time for background—5 s, analyte—10 s. The following standard reference materials (SRM) were used for calibration: albite (Na), olivine (Mg), pyrope (Al), diopside (Si, Ca), orthoclase (K), ilmenite (Ti), chromite (Cr), spessartine (Mn), trevorite (Fe, Ni), sphalerite (Zn), and shcherbinaite (V). High-resolution electronic images of rock and mineral textures were obtained in backscattered electron mode.

Raman spectra of feldspars from reaction zones of pyroxenes and veinlets in interstitial space were obtained using WITec Alpha 300R confocal Raman spectrometer equipped with

532 nm laser and three gratings (300, 600, and 1800 grooves/mm). The laser was focused through a 100× Zeiss objective.

Trace-element concentrations in primary silicate minerals (olivine, orthopyroxene, clinopyroxene) were determined in polished thick (~150–200 μm) sections by laser ablation inductively coupled plasma mass spectrometry (LA-ICP-MS) using an Analyte Excite analytic 193 ArF excimer laser ($\lambda = 193 \text{ nm}$) with Helex II ablation cell and Agilent 7900 quadrupole ICP-MS. SRM NIST 612 was used for the initial calibration, while SRM BCR-2G (basalt glass) was used to control the quality of analysis. All samples and standards were analyzed at the same measurement conditions: background measurement—20 s, sample analysis—40 s, laser beam diameter was 110 μm, energy 3.5 J/cm², pulse frequency—10 Hz. The flow values of cooling gas, plasma-forming gas, and additive gas (Ar) were 16.0, 1.0, and 1.0 L/min respectively. Helium with a purity of 6.0 and a flow rate of 1.0 L/min was used as a carrier gas. The energy of the plasma was 1550 W. Element concentrations were calculated using the “Iolite” software (version 4.7) [24,25]. ²⁹Si was used as an internal standard to calculate trace element abundances using SiO₂ abundances previously obtained by EPMA.

Determination of trace element content in small mineral grains of pyroxenes from reaction zones, unreacted parts of pyroxene grains, and a number of primary pyroxenes were determined by secondary ion mass spectrometry (SIMS) using Cameca IMS 4F ion microprobe at the Institute of Microelectronics of the Russian Academy of Sciences (Yaroslavl, Russia). Experiment conditions: focused primary beam of O₂⁺ ions with energy of 14.5 keV, diameter of 20 μm, and primary ion current of 8 nA. Each measurement included five cycles of signal accumulation, and the total time of analysis for one point was about 50 min. NIST 610 was used as calibration standard. The obtained signal was normalized to ³⁰Si and SiO₂ content determined by EPMA. Corrections for Gd, Yb, Eu, and Er were calculated according to the method of [26]. Analyses of primary clino- and orthopyroxene performed by LA-ICP-MS and SIMS in the same samples yielded comparable results for both methods.

The concentrations of major elements in whole-rock samples were obtained by X-ray fluorescence (XRF) analysis using Bruker S8 Tiger spectrometer. To perform the analysis, the rock powders (~110 mg weight) were fused with a mixture of lithium metaborate and lithium tetraborate with the addition of LiBr solution. The methodology is described in [27]. Abundances of alkaline elements (Na, K) have been further verified using the flame photometric method with LOMO DFS-12 spectrophotometer, which has low detection limits (Na 0.03 wt.%, K 0.01 wt.%).

The concentrations of trace elements in whole-rock samples were acquired by inductively coupled plasma mass spectrometry (ICP-MS) technique. Powdered samples (50 mg) were decomposed in a mixture of concentrated nitric and hydrofluoric acids (1:2) for 7 days at 110 °C. The analyses were performed using PerkinElmer Nexion300D quadrupole mass spectrometer.

EPMA, SEM, XRF, flame photometry, and ICP-MS measurements were performed at the Center for Isotope-Geochemical Studies of the Vinogradov Institute of Geochemistry, Siberian Branch of the Russian Academy of Sciences (IGC SB RAS, Irkutsk, Russia). LA-ICP-MS and Raman spectroscopy measurements were performed at the Center for Geodynamics and Geochronology of the Institute of the Earth’s Crust, Siberian Branch of the Russian Academy of Sciences (IEC SB RAS, Irkutsk, Russia).

4. Results

4.1. Petrography

The studied xenoliths are spinel lherzolites. They have medium-grained protogranular textures. The rocks do not demonstrate strain features, such as an undulose extinction in olivine. Olivine and orthopyroxene both have similar size of ~2 mm, but some samples contain rare larger (up to 6 mm) orthopyroxene. Clinopyroxene has smaller size (up to 1 mm). The pyroxenes do not contain exsolution lamellae. Spinel has an irregular shape and occurs in an interstitial space. The modal compositions of peridotite xenoliths are:

olivine (55.4%–61.0%), orthopyroxene (22.7%–28.9%), clinopyroxene (10.8%–18.6%), and spinel (1.8%–3.5%). Accessory sulfides have size up to first dozens of μm and occur both as inclusions in silicate minerals and as grains in interstitial space and reaction zones of pyroxenes. Carbonates and hydrous minerals such as amphibole and phlogopite are absent. Olivine grains lacks hydrous (e.g., serpentine, chlorite) or carbonate alteration. Close to basanite/xenolith contact, olivine sometimes contains trails of small inclusions ($\sim 1\text{--}10\ \mu\text{m}$) composed of feldspar and/or sulfide.

In all of the studied samples, the minerals exhibit reaction rims and thin veinlets in the interstitial space. The assemblages of primary and reaction minerals and their indexes are listed in Table 1.

Table 1. Summary of the mineral assemblages of Tumusun lherzolites.

Description	Mineral Index
Primary minerals without reaction zones	Ol, Opx, Cpx, Sp
Cores of minerals with reaction zones	Ol1, Opx1, Cpx1, Sp1
Olivine reaction zone	Ol2
Orthopyroxene reaction zone of first type	Ol3, Cpx3, Fs2
Orthopyroxene reaction zone of second type	Opx2, Fs2
Clinopyroxene reaction zone	Ol4, Cpx2, Fs1
Cr-spinel reaction zone	Sp2, Fs3
Veinlets in interstitial space	Fs

Note: Ol—olivine, Opx—orthopyroxene, Cpx—clinopyroxene, Sp—Cr-spinel, Fs—feldspar.

The olivine (Ol1) has a 50–100 μm wide reaction zone at the direct contact of xenolith with basanite. The reaction zone shows undulated border and is represented by olivine of different composition (Ol2) (Figure 2a).

The orthopyroxene (Opx) in direct contact with basanite has preserved only small areas of Opx1 surrounded by orthopyroxene reaction zone of the first type with width up to hundreds of μm (see Figure 2b). The reaction zone of Opx1 is composed of intergrowth of small subhedral grains of olivine (Ol3) and clinopyroxene (Cpx3) and vermicular aggregates of alkali feldspar. The proportions of olivine, clinopyroxene, and alkali feldspar in the reaction zone are circa 50:40:10%, respectively. Spinel (Sp3) and pentlandite are also found in these reaction zones. The border between the reaction zone and orthopyroxene is sharp.

Orthopyroxene at a distance of $\sim 2\ \text{mm}$ from basanite/xenolith contact also has preserved areas of Opx1 surrounded by complex reaction zone, consisting of two parts. A smaller part of the reaction zone is made of Ol3, Cpx3 and alkali feldspar, similar to the reaction zones at basanite/xenolith contact. A larger part of the reaction zone is hereafter referred to as orthopyroxene reaction zone of second type. It is composed of small orthopyroxene grains (Opx2), divided by vermicular aggregates of alkali feldspar (see Figure 2c).

In all samples, from basanite/xenolith contact toward the central part of xenoliths, the orthopyroxene reaction zones become narrower (see Figure 2d). In the central parts of the largest xenoliths, the reaction zone of orthopyroxene is absent, or developed not around the whole grain, and is similar to an interstitial aggregate (see Figure 2e,f,i,l). The reaction zones of orthopyroxene could have “zoning”—those parts of the reaction zone near to orthopyroxene are dominated by clinopyroxene, and those parts located far from orthopyroxene are dominated by olivine (see Figure 2e). In the central parts of xenoliths, the reaction zone of orthopyroxene is made only of olivine and alkali feldspar (see Figure 2f).

The reaction zone around clinopyroxene (Cpx1) is formed by the rim of secondary clinopyroxene (Cpx2), which contains vermicular aggregates of plagioclase and less abundant small grains of olivine (Ol4) and spinel (Sp4). Scarce grains of pentlandite are also present in the clinopyroxene reaction zone. The transition from central part of clinopyroxene to the reaction zone is sharp (see Figure 2g,h). These clinopyroxene microtextures in xenoliths are described as “spongy” or “sieve” [5,6,10,28]. The width of the clinopyroxene reaction zone varies and is maximal at the basanite/xenolith contact and at contact with

orthopyroxene reaction zone. In the closely located crystals of clinopyroxene, the width of reaction zone can be different. Toward the center of xenoliths, the width of clinopyroxene reaction zone become narrow (10–30 μm; Figure 2h) until its location only at certain crystal sides or complete disappearance (see Figure 2i,l).

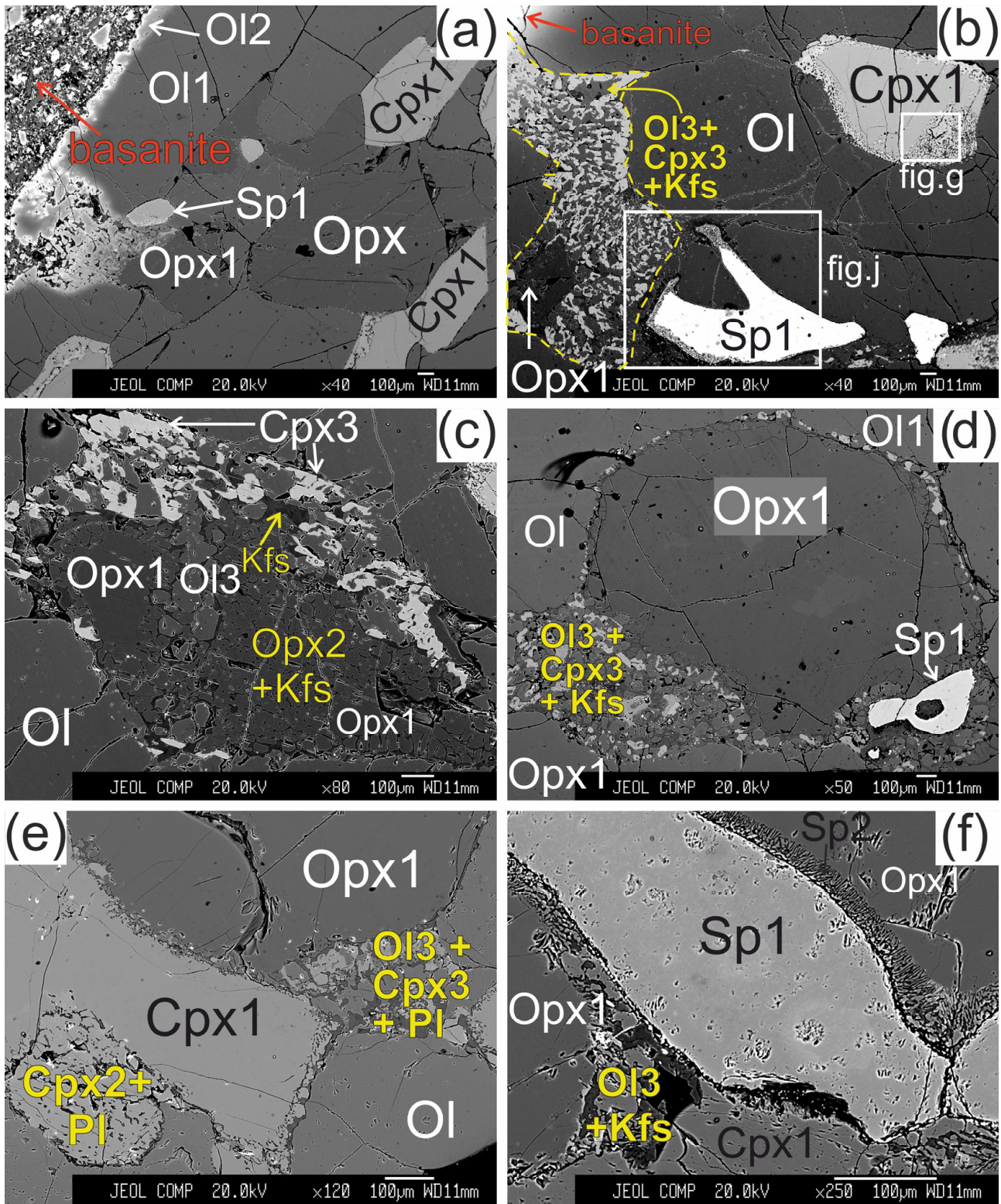


Figure 2. Cont.

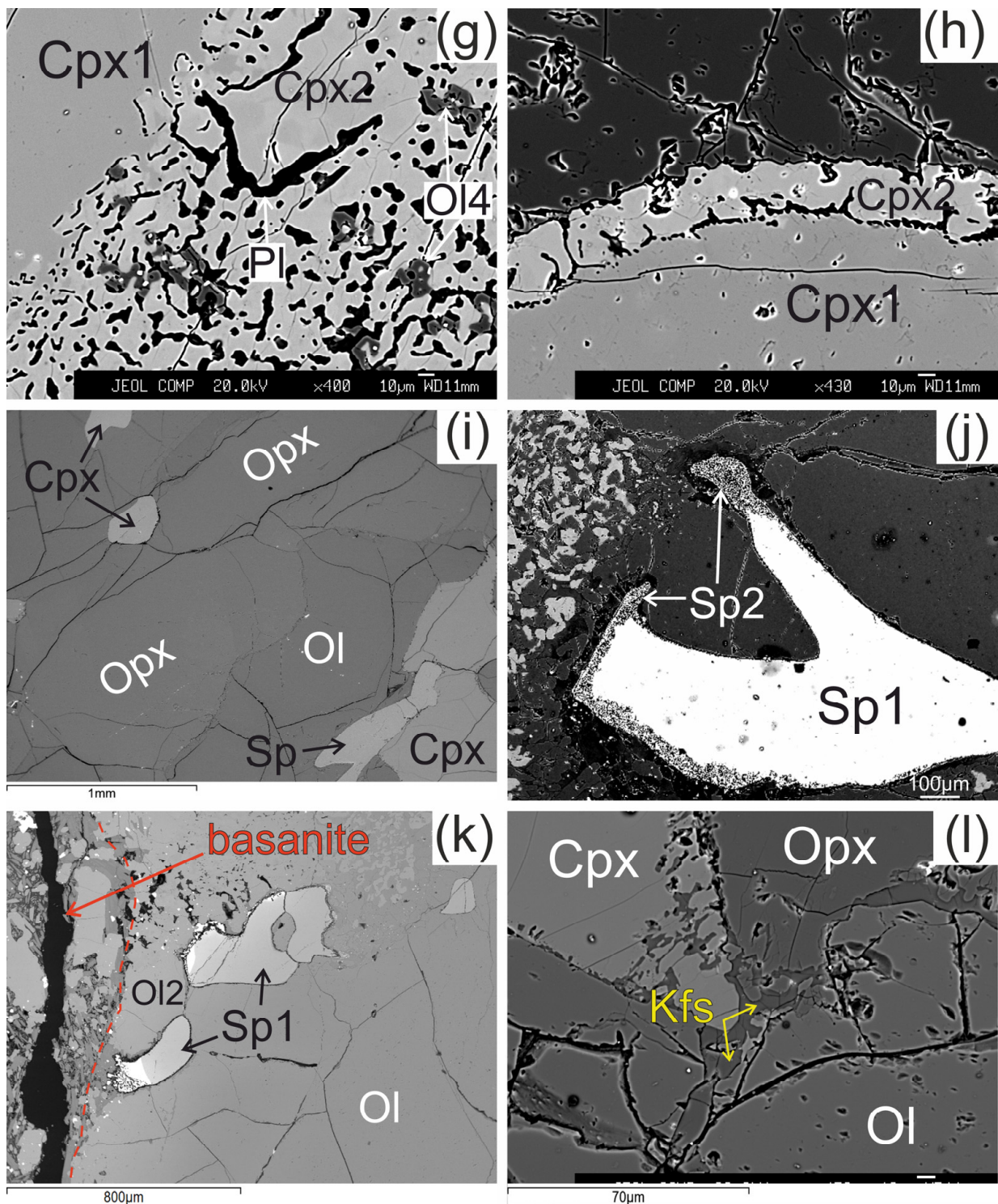


Figure 2. Microstructural features of Iherzolite xenolith of Tumusun volcano (back-scattered electron images). (a) Development of Ol2 rim after Ol1 at basanite/xenolith contact. Opx has wide reaction zone. Cpx has wider reaction zones on the grain boundaries oriented towards the contact. (b) Grain of orthopyroxene located close to basanite/xenolith contact and composed of non-reacted Opx1 and orthopyroxene reaction zone represented by secondary olivine (Ol3), clinopyroxene (Cpx3), and alkali feldspar (Kfs). The yellow dashed line shows the border of former orthopyroxene grain. Spinel (Sp1) has reaction zones at the contact with orthopyroxene. Clinopyroxene (Cpx1) has a reaction zone

of different width. The areas within the two rectangles are shown at higher magnification in the Figure 2g,j, respectively. (c) Orthopyroxene reaction zone of second type, located at distance of 2 mm from the basanite/xenolith contact. Unreacted Opx1 is surrounded by secondary Opx2 intergrown with vermicular Kfs. These aggregates are cut by a chain of secondary Ol3. A smaller part of the reaction zone is made of Ol3, Cpx3, and Kfs. (d) Orthopyroxene grain with a thin reaction zone located at some distance from basanite/xenolith contact. (e) Zoned reaction zone (Ol3+Cpx3+Pl) irregularly developed around orthopyroxene inside xenolith. (f) Reaction zone of orthopyroxene (Ol3+Kfs) without secondary clinopyroxene, and reaction zone of spinel inside xenolith. (g) Detailed image of clinopyroxene reaction zone composed of Cpx2 with inclusions of Ol4 (grey) and plagioclase (Pl, black) from Figure 2b. (h) Detailed image of clinopyroxene reaction zone from Figure 2f. (i) The center of large xenolith without reaction zones of pyroxenes and spinel. (j) Detailed image of spinel reaction zone from Figure 1b. The spinel reaction zone is composed of Kfs and secondary spinel (Sp2) intergrowth and is observed only next to the contact with the orthopyroxene reaction zone. (k) Reaction zones of spinel at basanite/xenolith contact. The red dashed line marks the contact between lherzolite xenolith and host basanite. (l) Veinlet of K-feldspar inside xenolith. (a)—sample HD52; (b–d,g)—sample HD5; (h,i,k)—sample HD24/2; (l)—sample HD38; (e)—sample HD6/1; (f)—sample HD6/2.

The reaction zone of spinel (Sp1) is represented by intergrowth of small subhedral spinel (Sp2) and alkali feldspar. Such spinel microtexture was described as “sieve” texture [6,28]. It is developed either at basanite/xenolith contact or at contact with the orthopyroxene reaction zone or feldspar veinlets (see Figure 2j,k). In other cases, the reaction zone of spinel is absent. This is observed at margins or in central parts of xenoliths.

In central parts of xenoliths, there are thin (up to 10 μm) veinlets of alkali feldspar, located between grains of minerals (see Figure 2l).

4.2. Mineral Composition

Hereafter, we use the term primary mineral, meaning the mineral without a reaction zone.

Primary olivine (Ol) is homogenous and has the same composition at margins and in the centers of xenoliths (Figure 3, Electronic Supplementary Table S1). The central parts of olivine grain (Ol1) rimmed by Ol2 have the same composition as primary olivine. Olivine has the composition common for the fertile mantle lherzolites, and on the Mg# (Mg/(Mg + Fe))—NiO plot, the composition points are located within the mantle array (Figure 3). Olivine of reaction rims (Ol2) has notably lower Mg# (0.73–0.78) and NiO (0.13–0.16 wt.%) and higher CaO (0.31–0.46 wt.%) compared to grain cores (Mg# 0.91, 0.38 wt.% NiO, 0.08 wt.% CaO) (Figure 3, sample HD-52, Electronic Supplementary Table S1). Ol2 is similar to olivine phenocrysts from basanite. Ol3 from orthopyroxene reaction zone near basanite/xenolith contact has low Mg# (0.78–0.81), relatively low NiO (0.1–0.18 wt.%), and relatively high CaO (0.22–0.28 wt.%), i.e., similar in composition to olivine phenocrysts in basanite. Within a single reaction zone, over a distance of ~ 500 μm from basanite contact inward xenoliths, there is a growth in Mg# in Ol3 until Mg# became similar to that in primary olivine. At the same time, NiO is lower and CaO is higher in Ol3 compared to the composition of primary olivine (Figure 3, samples HD38 and HD52, delineated by a dashed line). In the central parts of xenoliths, orthopyroxene reaction zones are narrow and their Ol3 has a composition similar to that of primary olivine (Figure 3, Electronic Supplementary Table S1).

In reaction zones of clinopyroxene at basanite/xenolith contact, Ol4 has low Mg# (0.82) and NiO (0.21 wt.%) and high CaO (0.22–0.45 wt.%) (see Figure 3, sample HD38; Electronic Supplementary Table S1). In clinopyroxene reaction zones inside the xenoliths, Ol4 has Mg# close to that of primary olivine, while NiO is similar to or lower and CaO is close to or higher than that of Ol1 (see Figure 3; Electronic Supplementary Table S1).

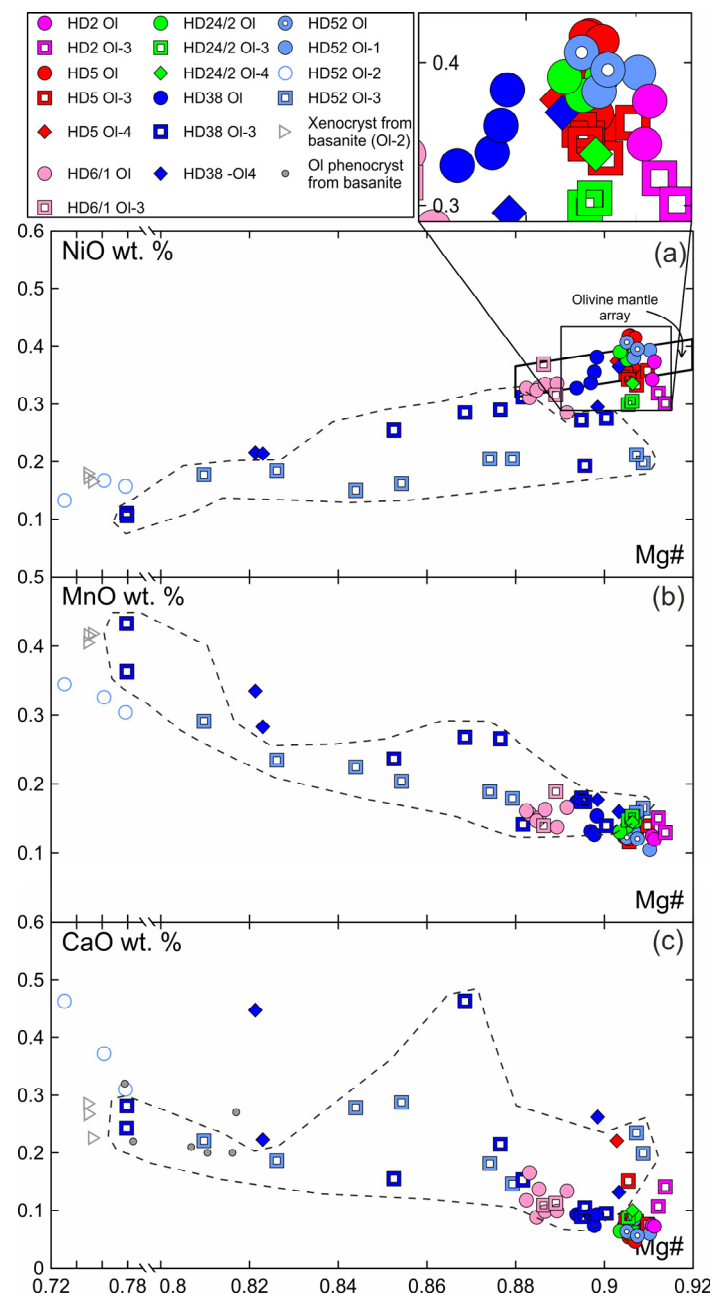


Figure 3. Composition of olivine from Tumasun lherzolite xenoliths. (a) NiO-Mg#, (b) MnO-Mg#, (c) CaO-Mg#. OI—primary olivine, OI1—core of olivine with reaction zone at basanite/xenolith contact, OI2—secondary olivine from reaction zone of OI1, OI3—secondary olivine from reaction zone of Opx1, OI4—secondary olivine from reaction zone of Cpx1. The dashed line show compositions of OI3 from reaction zone of Opx1 located at basanite/xenolith contact.

Primary orthopyroxene (Opx) is homogeneous enstatite. At xenolith margins, non-reacted Opx1 is also homogenous and have composition similar to that of primary orthopyroxene from centers of xenoliths. Opx2 from the rare orthopyroxene reaction zone of the second type (Opx2 + Kfs; see Figure 2c) has lower Al₂O₃, higher Mg#, and higher CaO abundance (Figure 4; Electronic Supplementary Table S1).

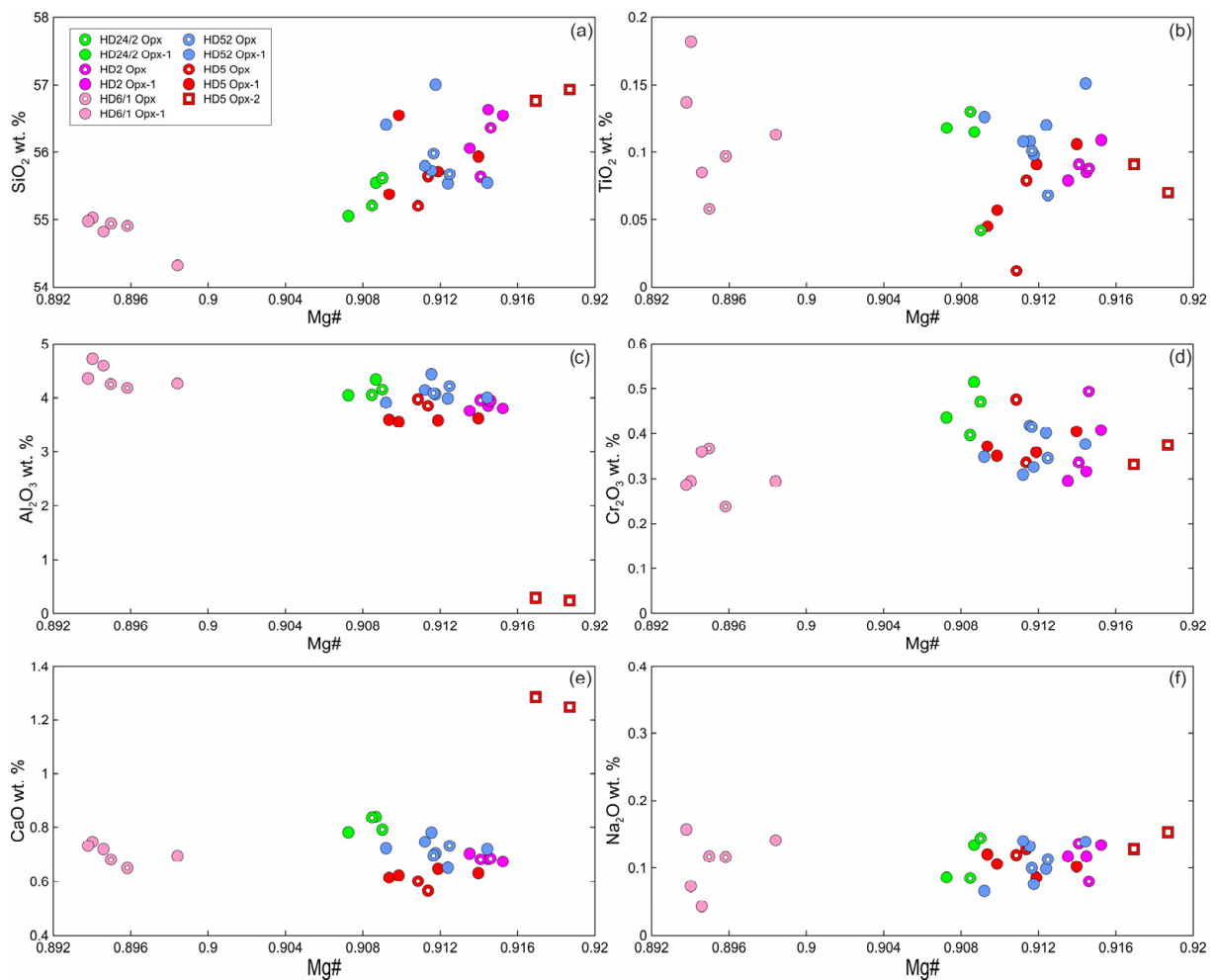


Figure 4. Composition of orthopyroxene from Tumasun lherzolite xenoliths. (a) SiO_2 -Mg# ($\text{Mg\#} = \text{Mg}/(\text{Mg} + \text{Fe}^{2+})$), (b) TiO_2 -Mg#, (c) Al_2O_3 -Mg#, (d) Cr_2O_3 -Mg#, (e) CaO -Mg#, (f) Na_2O -Mg#. Opx—primary Opx without reaction zones, Opx1—center of orthopyroxene with reaction zones, Opx2—secondary orthopyroxene from orthopyroxene reaction zones of the second type.

The primary clinopyroxene (Cpx) is an Al-Cr-diopside [29]. Non-reacted parts of clinopyroxenes (Cpx1) surrounded by reaction zone are homogenous and have the same composition as primary clinopyroxenes without reaction zones (Figure 5, Electronic Supplementary Table S1). The secondary clinopyroxene (Cpx2) of reaction zones of Cpx1 is diopside (Electronic Supplementary Table S1). Inside xenoliths, Cpx2 has a lower abundance of Al_2O_3 , $\text{Al}^{\text{VI}}/\text{Al}^{\text{IV}}$ ratio, and Na_2O and a higher abundance of SiO_2 and CaO compared to Cpx1. Cpx2 exhibits higher values of Mg#, TiO_2 , and Cr_2O_3 compared to those of Cpx1 (Figure 5). In the outer rim of a clinopyroxene grain that is in immediate contact with basanite, Cpx2 has low Mg#, Al_2O_3 , and Na_2O and high TiO_2 and CaO and is similar in composition to clinopyroxene phenocrysts from basanite (Figure 5, sample HD38, delineated by a dashed line). Cpx2 from the internal rim of the same grain has a composition similar to that of the Cpx2 located farther from basanite/xenolith contact (Figure 5).

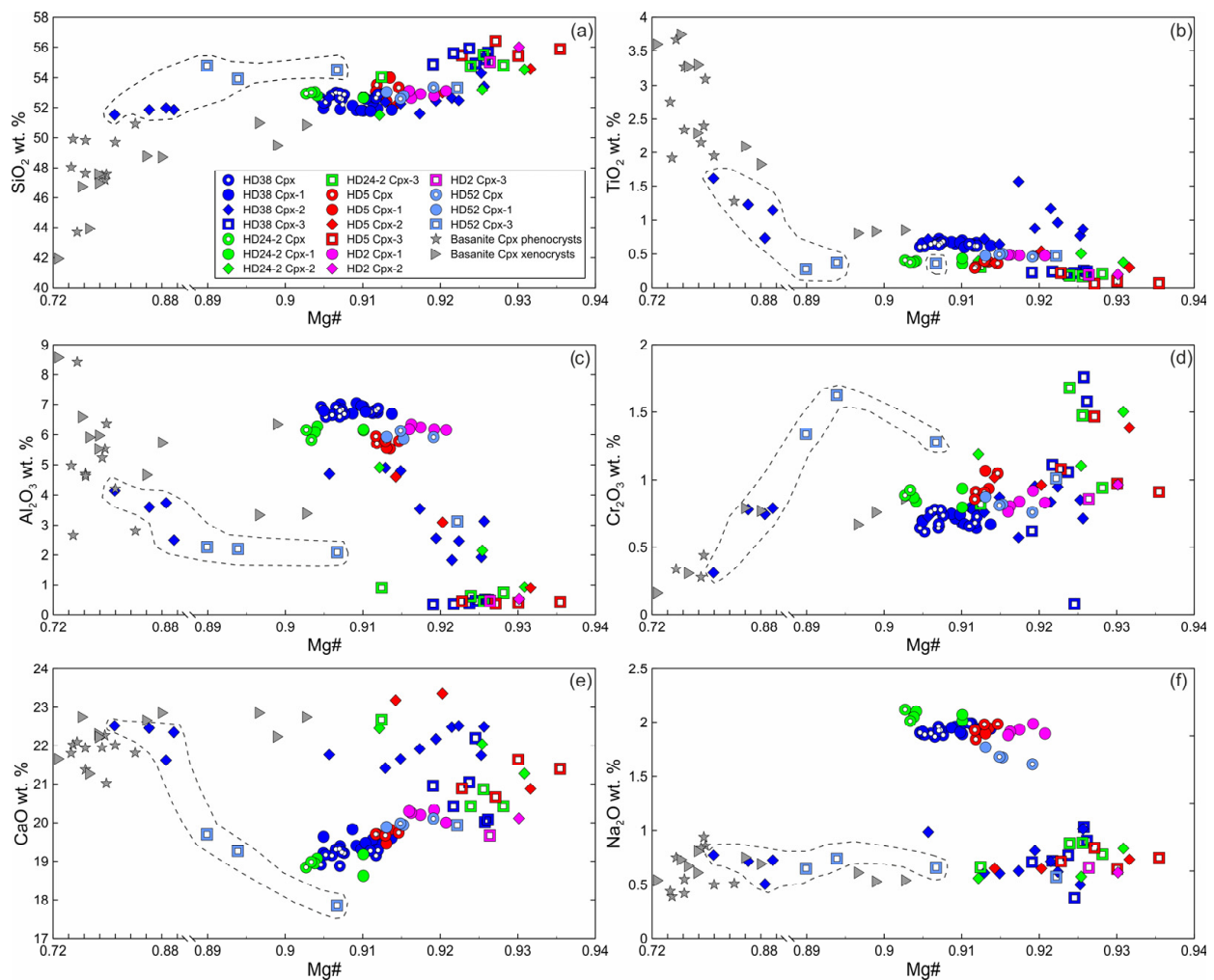


Figure 5. Composition of clinopyroxene from Tumusun lherzolite xenoliths. (a) SiO_2 -Mg#, (b) TiO_2 -Mg#, (c) Al_2O_3 -Mg#, (d) Cr_2O_3 -Mg#, (e) CaO-Mg#, (f) Na_2O -Mg#. Cpx—primary Cpx without reaction zones, Cpx1—core of clinopyroxene with reaction zones, Cpx2—secondary clinopyroxene from the reaction zone of Cpx1, Cpx3—secondary clinopyroxene from the reaction zone of Opx1. The dashed line shows compositions of secondary clinopyroxenes at basanite/xenolith contact.

Cpx3 from orthopyroxene reaction zones is augite (Electronic Supplementary Table S1). Composition of Cpx3 varies and depends on the position relative to basanite/xenolith contact. At a distance up to 100 μm from the contact, Cpx3 has lower Mg#, Al_2O_3 , and Na_2O , similar or lower CaO and TiO_2 , and higher SiO_2 and Cr_2O_3 compared to primary clinopyroxene (see Figure 5, sample HD52, delineated by dashed line). At a distance more than 100 μm from the contact, Cpx3 has higher Mg#, SiO_2 , and CaO and lower Al_2O_3 , TiO_2 , and Na_2O compared to Cpx1 (see Figure 5). Therefore, all secondary clinopyroxenes have lower Al_2O_3 and Na_2O abundances than primary Cpx.

Primary chromium spinel is homogenous within a single sample. Secondary spinel from reaction zones of spinel (Sp2) and orthopyroxene (Sp3) exhibits higher Cr# ($\text{Cr}/(\text{Cr}+\text{Al})$), TiO_2 , MnO, and V_2O_5 and lower Mg# and NiO compared to primary spinel (Electronic Supplementary Table S1).

Feldspar in reaction zones of orthopyroxene and spinel, as well as in veinlets between mineral grains is alkali feldspar (Figure 6a, Electronic Supplementary Table S1). Feldspar in reaction zones of clinopyroxene is plagioclase. Close to the basanite/xenolith contact, leucite is present in the reaction zones of pyroxenes (Electronic Supplementary Table S1).

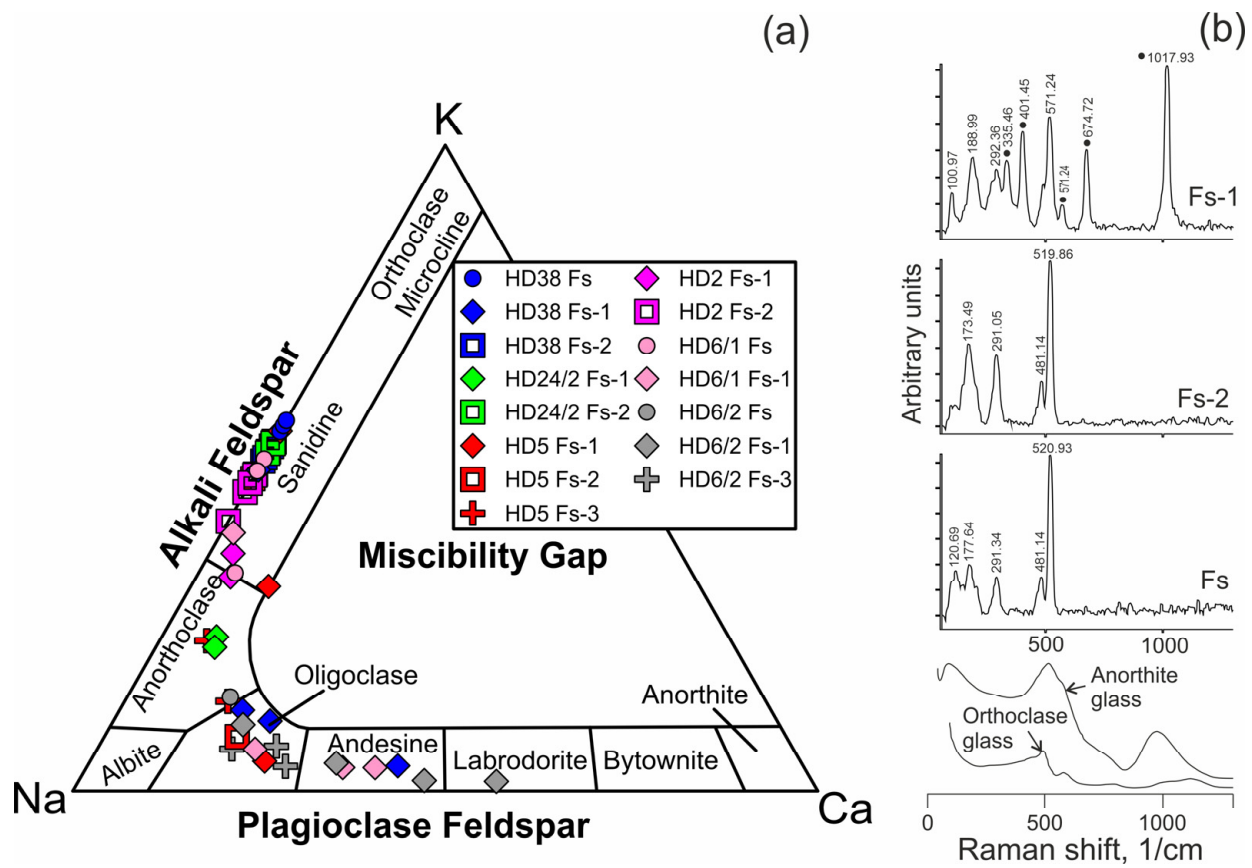


Figure 6. (a) Compositions of feldspar from Tumusun lherzolite xenoliths on the ternary classification diagram. Fs—feldspar from veinlets in interstitial space, Fs-1—feldspar from clinopyroxene reaction zones, Fs-2—feldspar from orthopyroxene reaction zones, Fs-3—feldspar from spinel reaction zones. (b) Raman spectra of feldspars from Tumusun lherzolite xenoliths. The spectrum of Fs-1 is influenced by signal of Cpx2 forming tight intergrowth with feldspar, and clinopyroxene Raman bands are marked by circles. Raman spectra of glasses of anorthite and orthoclase compositions [30] are shown for comparison.

Raman spectra of feldspar from orthopyroxene reaction zones as well as from veinlets in interstitial space resemble those of sanidine (Figure 6b). Raman spectra of feldspar from clinopyroxene reaction zones correspond to that of anorthite (see Figure 6b).

4.3. Whole-Rock Major and Trace Element Composition

The major and trace element whole-rock composition is listed in Table 2. In the three largest xenoliths, marginal and central parts have been analyzed. The peridotites possess abundances of SiO₂, MgO, Al₂O₃, CaO, and TiO₂ similar to that of primitive mantle. The marginal parts of xenoliths have evidently higher concentrations of K₂O and Na₂O compared to central parts, while the difference in other oxides is within analytical uncertainty. Small xenoliths, as well as margins of large xenoliths, have high K₂O and Na₂O, as pointed out earlier [10].

Table 2. Whole-rock and modal composition of lherzolite xenoliths.

Mode	HD5	HD6		HD24/2		HD34	HD38		HD58	HD68
Ol	64.0	55.4		58.6		58.9	57.3		55.7	61.0
Opx	21.0	23.0		28.9		22.7	23.1		25.8	25.0
Cpx	12.0	18.6		10.8		15.9	16.1		16.6	12.0
Spl	2.0	3.0		1.8		3.5	3.5		1.9	2.0
Center/ margin *	-	center	margin	center	margin	-	center	margin	-	-
SiO ₂	44.20	44.30	44.50	45.94	44.55	44.27	44.68	44.77	44.70	44.11
TiO ₂	0.08	0.17	0.16	0.10	0.10	0.17	0.17	0.16	0.15	0.10
Al ₂ O ₃	2.24	3.99	3.63	3.04	3.21	3.75	4.09	3.80	3.27	2.89
Cr ₂ O ₃	0.43	0.37	0.38	0.45	0.42	0.34	0.39	0.37	0.33	0.37
FeO *	8.16	8.54	8.37	7.62	7.78	8.5	8.01	8.09	8.20	8.22
MnO	0.17	0.14	0.15	0.13	0.13	0.13	0.14	0.14	0.16	0.15
MgO	40.90	37.32	38.16	39.86	40.96	38.45	38.26	38.80	39.00	40.36
CaO	2.77	3.52	3.38	2.53	2.39	3.28	3.52	3.23	3.24	2.55
Na ₂ O	0.44	0.42	0.46	0.26	0.30	0.39	0.32	0.35	0.35	0.24
K ₂ O	0.31	0.04	0.11	0.05	0.10	0.11	0.03	0.07	0.07	0.04
P ₂ O ₅	0.02	0.02	0.02	0.02	0.03	0.02	0.02	0.02	0.02	0.01
NiO	0.26	0.23	0.23	0.27	0.28	0.24	0.24	0.26	0.24	0.26
L.O.I.	0.00	-0.44	-0.28	-0.28	-0.10	-0.14	0.01	0.13	-0.18	-0.16
Total	99.98	98.63	99.28	99.99	100.15	99.51	99.88	100.19	99.55	99.14
Mg#	0.899	0.886	0.890	0.903	0.904	0.890	0.895	0.895	0.894	0.897
Rb	3.604	0.352	1.181	0.607	1.571	1.323	0.308	0.761	0.801	0.577
Ba	47.00	6.15	15.67	3.06	19.20	8.9	5.05	7.61	6.60	7.70
Nb	1.320	0.116	0.526	0.120	0.346	0.15	0.169	0.177	0.123	0.131
K	2600	300	1000	400	800	900	200	600	600	300
La	1.650	0.820	1.163	1.025	1.360	0.91	0.374	0.468	0.730	0.558
Ce	3.390	1.835	2.995	1.972	2.100	1.88	0.997	1.008	1.740	1.460
Pb	0.145	0.134	0.525	0.209	0.307	0.131	0.205	0.392	0.231	0.192
Pr	0.380	0.260	0.454	0.215	0.254	0.262	0.163	0.168	0.259	0.158
Sr	40.15	21.26	30.78	18.53	22.25	20.05	15.98	16.68	34.76	11.35
Nd	1.420	1.286	2.127	0.894	1.010	1.231	0.873	0.956	1.244	0.737
Zr	10.82	10.28	11.92	6.10	5.96	9.72	7.20	7.74	7.38	4.75
Hf	0.196	0.361	0.363	0.141	0.214	0.332	0.230	0.280	0.278	0.160
Sm	0.330	0.430	0.618	0.244	0.285	0.404	0.364	0.351	0.386	0.247
Eu	0.120	0.167	0.227	0.093	0.094	0.160	0.150	0.134	0.147	0.095
Ti	514.0	1341.6	1331.2	593.0	573.0	1206.0	992.0	934.7	1038.2	767.3
Gd	0.353	0.577	0.703	0.356	0.355	0.6	0.543	0.526	0.475	0.370
Tb	0.066	0.113	0.124	0.063	0.068	0.109	0.106	0.101	0.091	0.066
Dy	0.434	0.792	0.847	0.432	0.509	0.764	0.718	0.684	0.614	0.479
Ho	0.092	0.176	0.181	0.101	0.107	0.166	0.164	0.153	0.129	0.106
Y	2.47	4.79	4.18	2.28	2.72	4.55	4.18	3.70	3.43	2.87
Er	0.285	0.545	0.527	0.319	0.350	0.47	0.490	0.463	0.381	0.330
Tm	0.041	0.077	0.078	0.047	0.050	0.075	0.076	0.070	0.053	0.048
Yb	0.264	0.498	0.513	0.325	0.380	0.488	0.512	0.493	0.335	0.329
Lu	0.042	0.083	0.079	0.052	0.058	0.078	0.082	0.075	0.055	0.052

* Analysis of the center or margin of large xenoliths. Mg# = Mg/(Mg + Fe).

Most of the whole-rock compositions have primitive mantle-like trace element compositions, and multi-element plots demonstrate maximum of K and minimum Nb, while Pb, Sr, Zr, Hf, and Ti do not show systematic patterns (Figure 7b–f). In one sample, the trace elements show decrease in normalized abundances toward most incompatible elements, but have maxima of Ba, K, Pb, and Sr, and minima of Nb, Zr, Hf, and Ti (Figure 7a). In general, in the marginal parts of large xenoliths, the trace element pattern is similar to that of the central parts, but the marginal parts have higher abundances of LILE (Figure 7a–c). In addition, the marginal part of sample HD6 shows higher LREE-MREE

(Figure 7c). Overall, the studied Tumasun lherzolite xenoliths are fertile both in major and trace element composition.

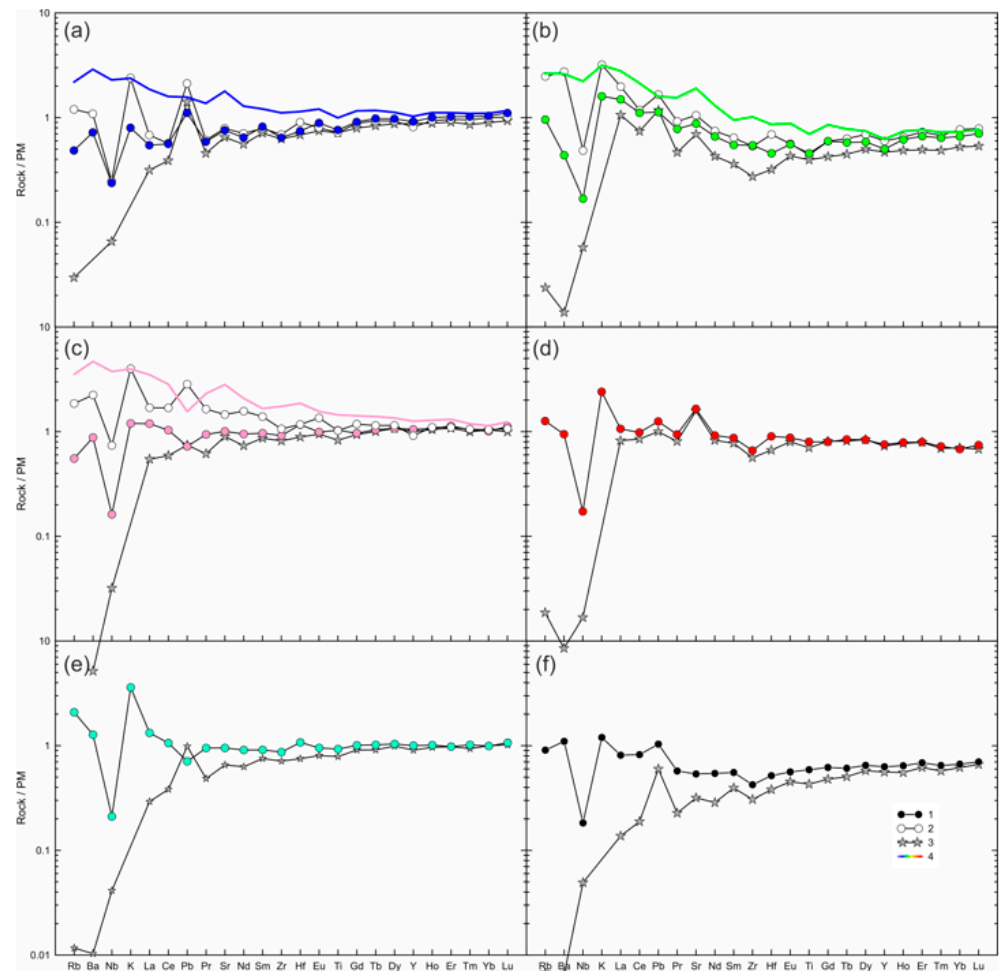


Figure 7. Measured and calculated trace element compositions of lherzolite xenoliths from Tumasun volcano normalized to the primitive mantle [31]. (a) HD38; (b) HD24/2; (c) HD6; (d) HD58; (e) HD34; (f) HD-68. 1—measured whole-rock composition of central part of xenolith (blue circle—HD38, green circle—HD24/2, pink circle—HD6, red circle—HD58, cyan circle—HD34, black circle—HD68); 2—measured whole-rock composition of marginal part of xenolith (only for (a–c)); 3—calculated whole-rock composition obtained from modal composition and trace element abundances in olivine, ortho- and clinopyroxene; 4—mix of compositions of the central part of lherzolite xenolith and basanite (see Section 5.2 for an explanation).

4.4. Mineral Trace Element Composition

The primary clinopyroxenes without reaction zones have two types of REE patterns. The first type demonstrates undifferentiated HREE-MREE and depletion in LREE, i.e., depleted pattern common for residual fertile lherzolites (Figure 8a). The normalized patterns of trace elements also show a depleted shape and depletion in the most incompatible elements (from Ba to Nd) and weak minima of Ti and Zr (Figure 8b). Inside xenoliths, clinopyroxene with thin reaction zones have the same spectrum type and abundances of trace elements in Cpx1 (core) and Cpx2 (reaction zone), resembling the composition of primary clinopyroxene without reaction zones, except for high Ba in Cpx2 (Figure 8d,e). In clinopyroxene grains located close to basanite/xenolith contact near the orthopyroxene reaction zone (Figure 8g,h) and at immediate contact with the basanite (Figure 8j,k), even Cpx1 has higher abundances of Ba and sometimes La and Ce, but abundances of other trace element are similar to that of primary clinopyroxene. The composition of Cpx2 varies.

Compared with Cpx1, Cpx2 has a gradual increase in trace element abundances toward the basanite/xenolith contact. In the internal part of the reaction zone, in Cpx2, the maxima of Ba, Sr, and Eu appear, and the minima of Zr, Hf, and Ti remain (Figure 8g–l; analyses #16, #8, #12). Further in the external part of the reaction zone, Cpx2 has higher trace element abundances combined with minima of Ba, Sr, and Eu (Figure 8g–l; analyses #17, #13, #14). It is notable that Cpx1 from the smallest xenolith (1.5 cm in length) has a depleted trace element pattern (Figure 9).

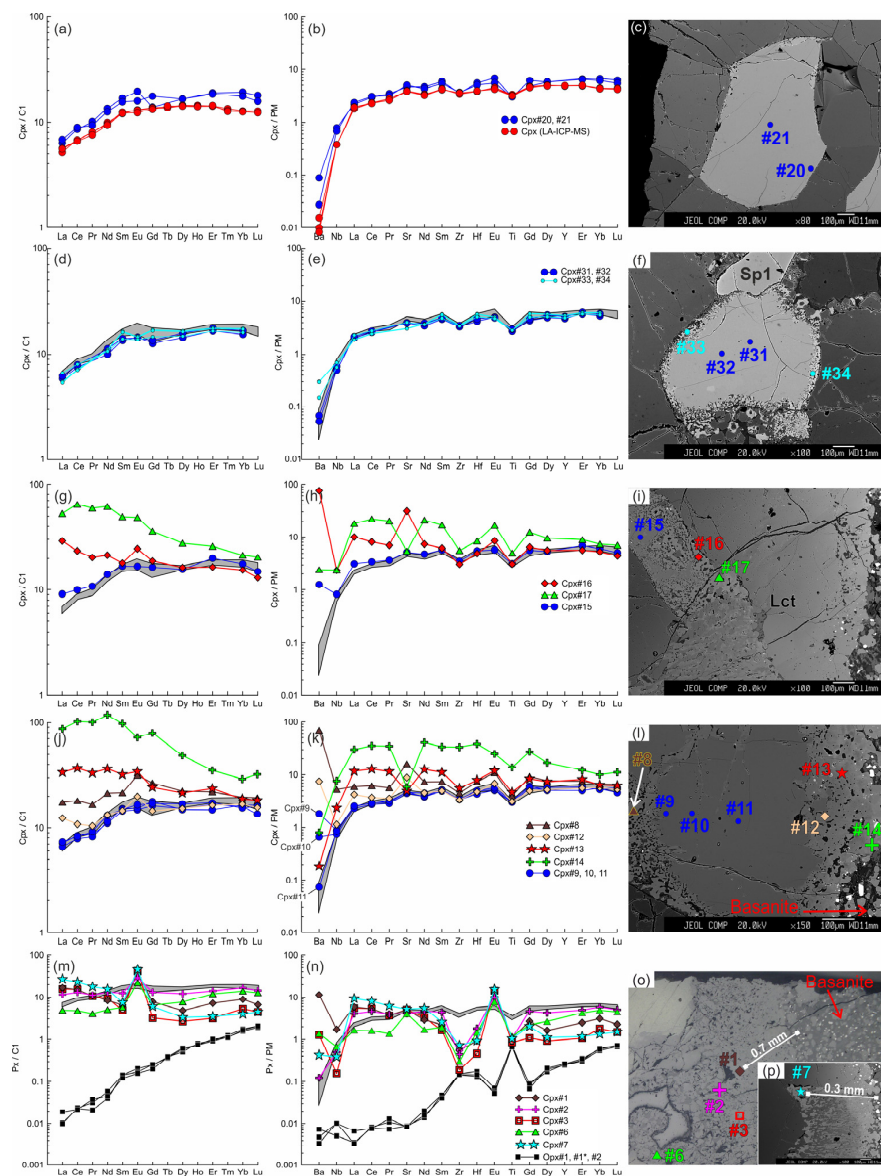


Figure 8. The trace element composition of the clino- and orthopyroxenes from sample HD38 normalized to the CI chondrite [31] (a,d,g,j,m) and primitive mantle [31] (b,e,h,k,n). (a–c) Primary clinopyroxene (#20, #21) without reaction zones. Trace element composition of primary clinopyroxene obtained by LA-ICP-MS is shown for comparison. (d–f) Cpx1 (#31, #32) with thin reaction zone of Cpx2 (#33, #34). In (d,e,g,h,j,k,m,n), the gray field shows the compositions of the primary clinopyroxene (#20, #21). (g–i) Cpx1 (Cpx#15) with a wide reaction zone of Cpx2 (Cpx#16, Cpx#17) near the basanite/xenolith contact. (j–l) Cpx1 (#9–11) with a wide reaction zone of Cpx2 (#12–14) at basanite/xenolith contact. (m–p) Cpx3 (#1–7) from the orthopyroxene reaction zone at basanite/xenolith contact. The location of the primary orthopyroxene (#1, #1*, #2) is beyond the sample areas shown on the photo.

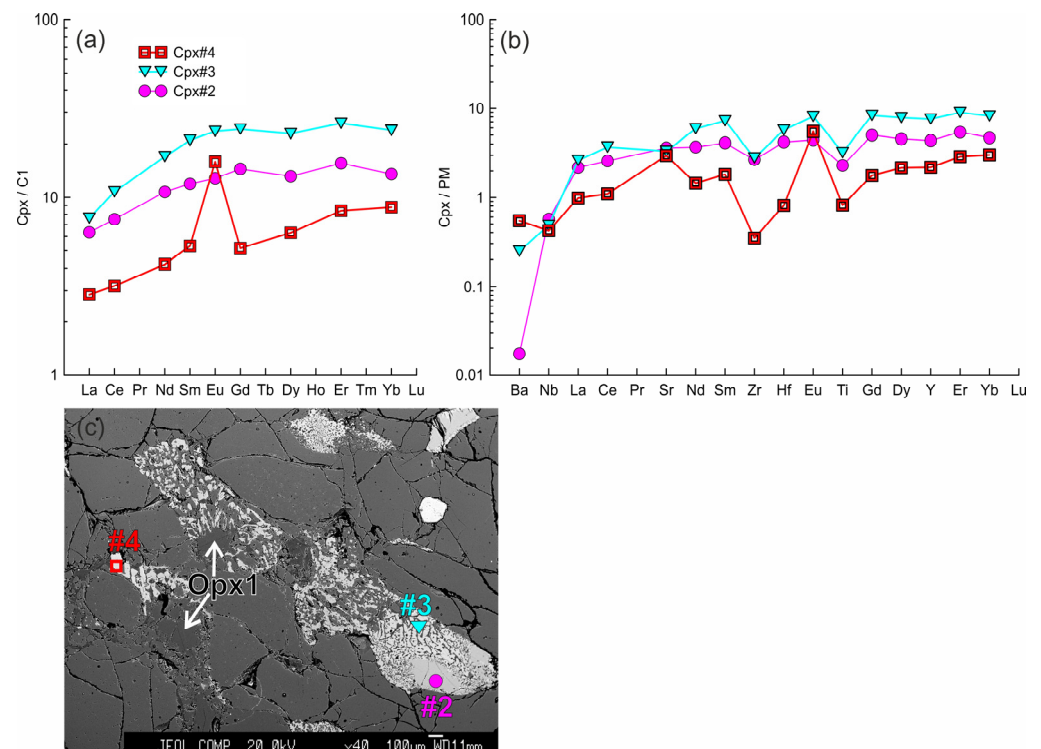


Figure 9. (a,b) The trace element composition of the clinopyroxenes and orthopyroxenes from sample HD2 (xenolith of 1.5 cm in size) normalized to the CI chondrite [31] (a) and primitive mantle [31] (b). Cpx 1 (#2) with a wide reaction zone of Cpx2 (#3) at contact with the orthopyroxene reaction zone. Cpx3 (#4) from the reaction zone of Opx1. (c) Image showing different widths of pyroxene reaction zones. Clinopyroxene located in the upper right corner contacts olivine only and shows a narrow reaction zone.

Cpx1 from some of the samples is enriched in LREE both near the center of the xenolith and at the basanite/xenolith contact (Figures 10a and 11a). External parts of Cpx1 show more Ba near the wider reaction zone (Figure 10e). Both Cpx1 and Cpx2 have similar REE patterns (Figures 10a,d and 11a). Cpx1 and Cpx2 normalized trace-element patterns demonstrate minima of Zr and Ti; Cpx1 shows minima of Ba and Nb, but Cpx2 has the maximum of Ba and sometimes Sr (Figures 10b,e and 11b).

In samples with LREE-enriched primary clinopyroxenes, Cpx3 is also enriched (Figures 10g and 11d,g). In samples with LREE-depleted primary clinopyroxene, Cpx3 can have both depleted (see Figure 9a) and enriched (see Figure 8m–o) trace-element pattern. In the last case, the enriched Cpx3 is located at distance up to 1 mm from basanite/xenolith contact. Trace element abundances in Cpx3 vary from the levels close to that of primary clinopyroxene to values transitional between primary orthopyroxene and clinopyroxene (see Figures 8m,n, 9a,b, 10g,h and 11d–h). The general characteristic of Cpx3 is the presence of positive Eu anomaly and negative anomalies of Nb, Zr, Hf, and Ti. Anomalies of Ba and Sr are either positive or lack. Weak negative Eu anomaly was revealed only in Cpx3 from thin reaction zone of orthopyroxene located far from basanite/xenolith contact (Figure 11g). Notably, in the same orthopyroxene reaction zone, there is Cpx3 with weak positive Eu anomaly. Moreover, Cpx3 from this reaction zone is distinct in higher REE abundances and minimum of Sr, compared to Cpx3 near the basanite/xenolith contact.

Orthopyroxenes are LREE-depleted in the samples with depleted-type clinopyroxenes (see Figure 8m). Orthopyroxenes in samples with LREE-enriched clinopyroxene show higher abundances of La and Ce compared to pattern common for depleted orthopyroxene (Figures 10g and 11d). On primitive-mantle-normalized plots, orthopyroxenes show maxima of Ti, Zr, and Hf, complementary to corresponding minima in clinopyroxenes (Figures 8n, 10h and 11e). LREE-enriched orthopyroxenes show minima in Ba, Nb, and Sr

(Figures 10h and 11e). In orthopyroxene with a reaction zone of the second type, Opx1 has similar trace-element abundances and pattern as primary orthopyroxene from the xenolith center, except for low abundances of Ba, La, and Ce and weak Eu maximum in the former (Figure 11j–l). At the same time, Opx1 preserves enriched type of REE pattern. Opx2 from this reaction zone has U-shaped normalized trace-element pattern with a gradual decrease from HREE to Zr, Sm, and Nd, and further growth in more incompatible elements, and is also characterized by maxima of Hf, Eu, and Ti (Figure 11j–l). Opx2 is enriched in highly incompatible elements, and have positive Eu anomaly and inhomogeneous composition, which is different from Opx1 in the same grain.

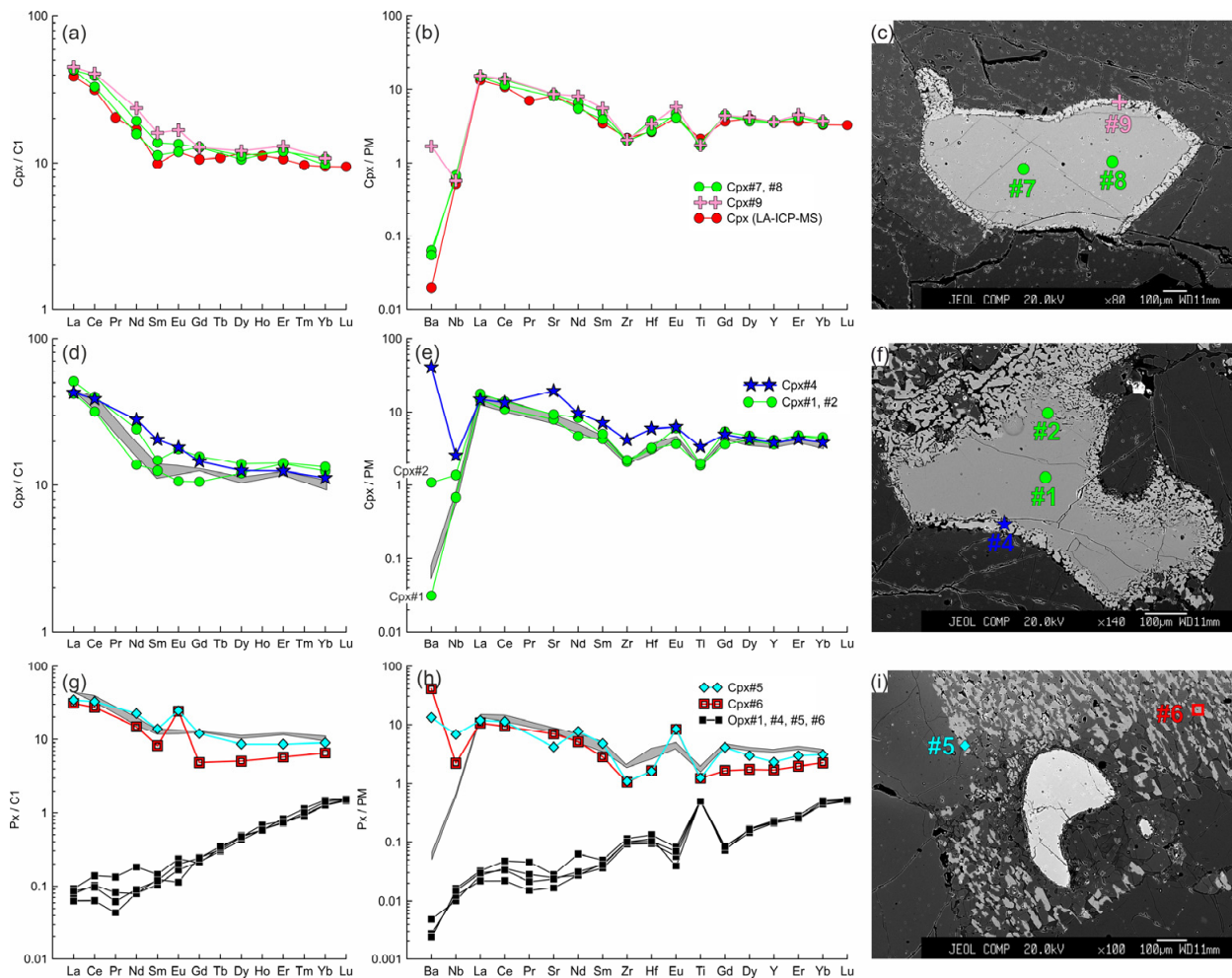


Figure 10. The trace element composition of the clinopyroxenes and orthopyroxenes from sample HD24-2 normalized to the CI chondrite [31] (a,d,g) and primitive mantle [31] (b,e,h). (a–c) Cpx1 (#7, #8) with thin reaction zone of Cpx2 (#9) near the center of the xenolith. Trace element composition of primary clinopyroxene obtained by LA-ICP-MS is shown for comparison. (d–f) Cpx1 (#1, #2) with a wide reaction zone of Cpx2 (#4) near the basanite/xenolith contact. In (d,e,g,h), the gray field shows the compositions of Cpx1 (#7, #8). (g–i) Cpx3 (#5, #6) from the orthopyroxene reaction zone located near the basanite/xenolith contact. Location of the primary orthopyroxene (#1, #4–6) is beyond the sample areas shown on the photo.

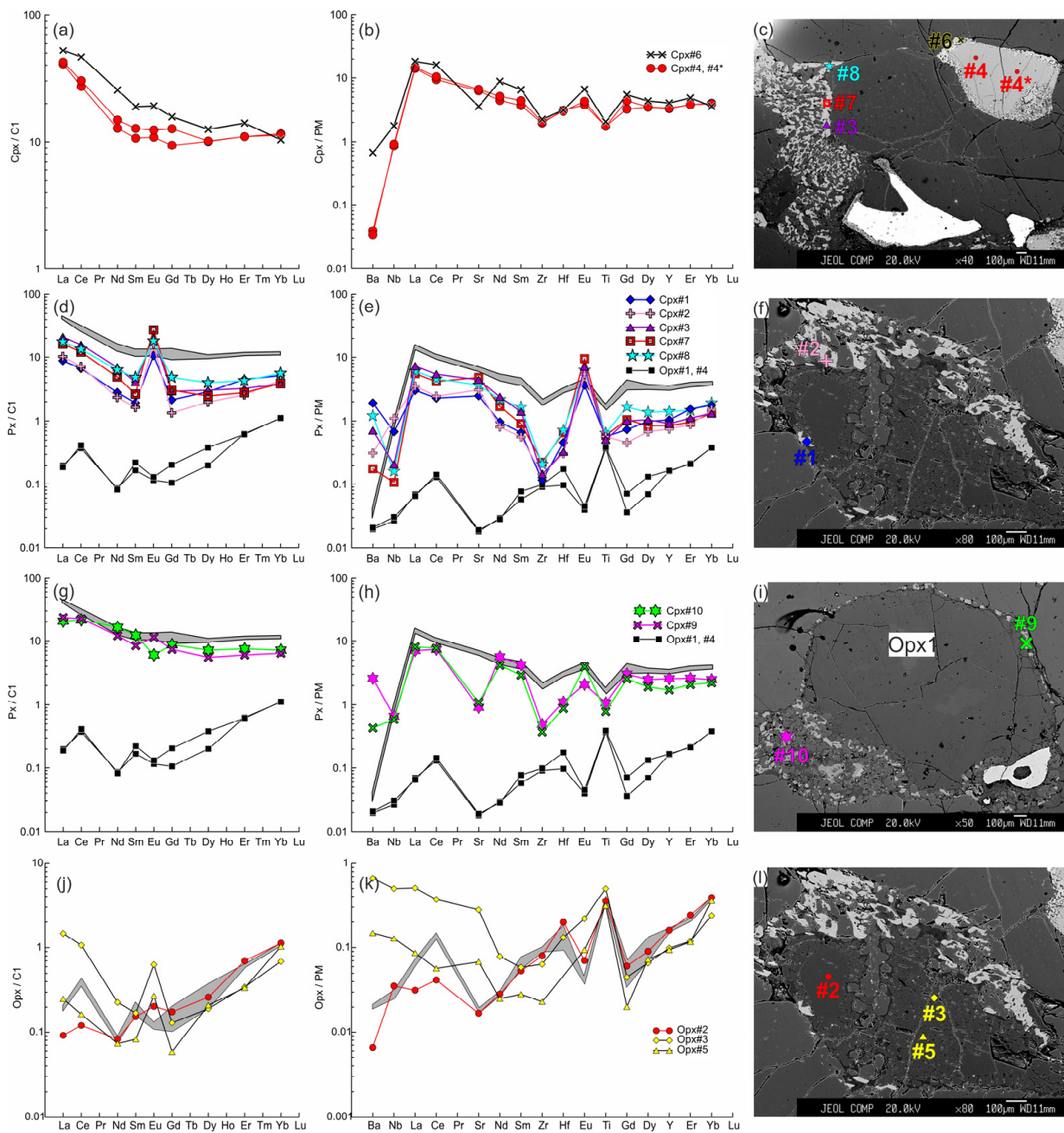


Figure 11. The trace element composition of the clino- and orthopyroxenes from sample HD5 normalized to the CI chondrite [31] (a,d,g,j) and primitive mantle [31] (b,e,h,k). (a–c) Cpx1 (#4, #4*) with a wide reaction zone of Cpx2 (#6) near the contact with basanite. (d–f) Cpx3 (#1, #2 in (f), #3, #7, #8 in (c)) from the orthopyroxene reaction zone, and primary orthopyroxene (Opx#1, #4; the location is beyond the area shown on the photo). In (d,e,g,h), the gray field shows the compositions of Cpx1 (#4, #4*). (g–i) Cpx3 (#9, #10) from the thin reaction zone of Opx1 inside the xenolith. (j–l) Orthopyroxene reaction zone of the second type, with unreacted Opx1 (#2) and secondary Opx2 (#3, #5). The gray field in (j,k) shows the compositions of the primary orthopyroxene (#1, #4).

5. Discussion

5.1. Formation of Reaction Zones in Minerals of Lherzolite Xenoliths of Tumusun Volcano

Microstructural characteristics observed in the Tumusun peridotites are often found in peridotite xenoliths in alkaline basaltic rocks worldwide [1,2,4,28,32–35]. However, the mineral reaction zones in xenoliths generally contain glasses but not feldspar, as

in case of Tumusun lherzolites, as found in [10] and the present work. At the same time, in peridotite xenoliths from other localities, glasses of similar composition were described, including those with feldspar stoichiometry and MgO-free [28]. In peridotite xenoliths from Vitim volcanic field basanites (Baikal Rift Zone), feldspar (sanidine and plagioclase) is found along with rare segregations of glass (up to 10–20 μm), both in interstitial space and as inclusions in minerals [36]. In the studied Tumusun samples, the largest vermicular aggregates found in mineral reaction zones are feldspar, and the rest of the aggregates are too small to be identified by petrographic methods. MgO was not detected and analyses yielded good stoichiometry, proving these aggregates to be feldspar. Additionally, Raman spectroscopy of several veinlets and vermicular aggregates in reaction zones of orthopyroxene and clinopyroxene detects they are feldspars (Figure 6b), i.e., crystalline phases, but not the glass. The glasses of sanidine and anorthite composition [30] exhibit wide Raman bands (Figure 6b) and differ markedly from crystalline alkali feldspar and plagioclase, whose characteristic Raman bands are narrow. The presence of feldspars (but not the glass) could be related to slow cooling. Thus, we can consider the feldspars of Tumusun peridotites as crystallized evolved melts, i.e., melts left after crystallization of secondary olivine, clinopyroxene etc.

In the studied samples, all minerals at basanite/xenolith contact have reaction zones. Toward the internal parts of the largest xenoliths, the mineral reaction zones gradually disappear (see Figure 2i). Therefore, the formation of mineral reaction zones could not be related to the mantle processes, but takes place during transportation of xenoliths by the basanite magmas up to the surface. The reaction zones did not form during mantle metasomatism under influence of alkali-rich and water-poor fluid, as suggested for Tumusun lherzolites by [10].

Lower Al_2O_3 , $\text{Al}^{\text{VI}}/\text{Al}^{\text{IV}}$ ratio, and Na_2O , but higher Mg# and CaO in clinopyroxene reaction rim compared with core sometimes are considered as evidence for the formation of secondary minerals due to partial melting [5,8]. However, in case of Tumusun lherzolites, Cpx2 has similar and, more often, higher TiO_2 than Cpx1, which does not correspond to the model of partial melting. Moreover, the petrographic observations preclude the decompression melting, since not all grains and not all grain sides of clinopyroxene and spinel have reaction zones (see Figure 2e,j,k, Figures 8c and 9c). The $\text{Al}^{\text{VI}}/\text{Al}^{\text{IV}}$ ratio in clinopyroxene is an indicator for the pressure. Cpx1 and primary clinopyroxene have similar $\text{Al}^{\text{VI}}/\text{Al}^{\text{IV}}$ ratios. Secondary Cpx2 and Cpx3 have similar to each other but systematically lower $\text{Al}^{\text{VI}}/\text{Al}^{\text{IV}}$ ratio than the primary clinopyroxene and Cpx1 (Electronic Supplementary Table S1). A low $\text{Al}^{\text{VI}}/\text{Al}^{\text{IV}}$ ratio reflects formation of secondary clinopyroxenes at low pressure, but does not reflect decompression melting.

Inside xenoliths, the cores of clinopyroxene grains with reaction zone have the same major and similar trace element composition as clinopyroxenes without the reaction zone (see Figures 8a–f and 10a–f). Moreover, Cpx2 of reaction zone also demonstrates similar trace element composition, except for high Ba and sometimes Sr (see Figures 5, 8a–e and 10a–e). This is possible only in case of Cpx2 formation from dissolved part of a clinopyroxene grain but not in case of partial melting of the clinopyroxene grain, because in the second case, there must be changes in composition of residual clinopyroxene in accordance with the partition coefficients. The higher values of Ba and Sr in Cpx2 point at the presence of an interacting melt which dissolves clinopyroxene. Rarely observed orthopyroxene reaction zone of second type with the presence of Opx2 (see Figure 2c) is similar to the reaction zones of clinopyroxene. Opx2 is not residual, because it has higher abundances of highly incompatible elements (including Nb) compared to Opx1. This reflects the participation of an additional melt in the formation of Opx2 (see Figure 11j–l). The process of dissolution (but not the melting) is confirmed by the lack of compositional changes in Opx1 relative to the primary orthopyroxene without reaction zones. The formation of Opx2-bearing reaction zone is possible due to incongruent dissolution of orthopyroxene.

The composition of secondary minerals of reaction zones in xenolith margins clearly reflects the basanite participation in their formation. For example, closer to the basan-

ite/xenolith contact, Mg# of olivine (Ol2, Ol3, Ol4) and clinopyroxene (Cpx2, Cpx3) decrease to the values observed in corresponding basanite phenocrysts (Figures 3 and 5). The above changes in Mg# occur in reaction zone of olivine, orthopyroxene, and clinopyroxene at a distance of ~100 to 200 μm from basanite/xenolith contact. Moreover, in Cpx2 of the reaction zone (with width of ~200 μm) in contact with basanite, there is a considerable growth in trace elements toward the contact, which reflects diffusional exchange with the basanite (Figure 8j–l). Cpx2 located at direct basanite/xenolith contact shows geochemical features common for clinopyroxene phenocrysts from alkaline basalts [37], such as trace element abundances and normalized trace element pattern, including negative anomalies of Ba, Nb, Sr, and Ti.

Cpx3 from orthopyroxene reaction zone located at distance of ~0.3 to 1 mm from basanite/xenolith contact is different from Cpx2 from the contact both in lower abundances and normalized pattern of trace elements. Therefore, this Cpx3 cannot crystallize directly from basanite melt. At the same time, Cpx3 has higher Mg# than the primary clinopyroxene. This suggests crystallization of Cpx3 from a melt formed due to orthopyroxene dissolution. Cpx3 shows higher abundances and different normalized pattern of trace elements (LILE- and LREE-enriched) compared to that of primary orthopyroxene, which has a depleted trace-element pattern (Figure 8m–o). The values of Cpx/melt partition coefficients for REE vary and depend on melt composition (abundances of SiO_2 and $\text{Na}_2\text{O}+\text{K}_2\text{O}$), and could be higher than unity [38,39]. However, Cpx/melt partition coefficients for LREE are lower than for HREE; therefore, to explain the observed LREE-enrichment in Cpx3, the parental melt has to be LREE-enriched. The abundances of Zr and Ti in Cpx3 are similar, and Nb is higher compared to the composition of primary orthopyroxene (Figure 8m,n). Considering that Cpx/melt partition coefficients for Zr and Ti are less than unity and do not increase with increasing SiO_2 content of melt [38], we can expect some gain of HFSE from basanite. Since diffusion coefficients for HFSE are lower than that for HREE [40,41], one can also expect input of HREE in this process. This would not be observed if only primary orthopyroxene contributed to the trace-element budget of the melt. This suggests that not only LILE and LREE, but also some amount of HREE and HFSE, was added from basanite to the melt from which Cpx3 was crystallized. These arguments are conformed to diffusion coefficients of chemical elements of mafic and felsic melts, which are the highest for LILE (corresponding to that of Ca), moderate for REE (decreasing from La to Lu except Eu) and minimal for HFSE [40,41]. The diffusion of Eu is faster than for the rest REE, which is related to presence of some amount of Eu^{2+} in the melt [41]. This explains the positive Eu anomalies in secondary Cpx3 of orthopyroxene reaction zones. Such positive Eu anomalies in the secondary clinopyroxenes from reaction zones are reported for peridotite xenolith from Cenozoic alkaline basalts in Xilong, South China [2], though generally, the positive Eu anomaly in clinopyroxene is unusual.

Petrographic observations provide the evidence of melt circulation inside peridotite xenoliths and melt interaction with minerals. This is expressed in the following: (1) reaction zone formation not around all sides of Opx, Cpx, and Sp grains; (2) the reaction zones of clinopyroxene and spinel are wider in contact with orthopyroxene reaction zones (see Figures 2b and 9c); (3) occurrence of thin veinlets of feldspar (see Figure 2l). At the same time, the olivine located inside xenoliths is not zoned, i.e., its reaction zones lack. Therefore, the basanite melt does not penetrate inside lherzolite xenoliths, and the melt circulating inside xenoliths has a different composition. This follows from the composition of secondary minerals in reaction zones. Ol3 from orthopyroxene reaction zone is similar to primary olivine except for lower NiO in Ol3 (see Figure 3), and both Cpx2 and Cpx3 are more magnesian than primary clinopyroxene (see Figure 5). In clinopyroxene grain in contact with basanite, Ol4 from the internal (at xenolith side) reaction zone already has Mg#, as in primary olivine (see Figure 3, sample HD38). The trace element pattern of secondary clinopyroxene inside xenoliths is distinct from that of secondary clinopyroxene at basanite/xenolith contact. Cpx2 and Cpx3 of grains, located far from the contact inherit depleted or enriched type of REE distribution from primary pyroxenes of the sample.

Moreover, the composition of melt is changing inside xenoliths. This is reflected in varied mineral composition of orthopyroxene reaction zones (presence or absence of clinopyroxene), the difference of feldspar composition in reaction zones of different minerals, and wide variations of major-element compositions (Mg#, Al_2O_3 , TiO_2 , Cr_2O_3) of secondary clinopyroxenes. Even within a single reaction zone, Cpx3 has wide variation in trace element abundances, testifying the high heterogeneity of the parental melt. The melt is inhomogeneous because the xenolith-forming minerals (orthopyroxene, clinopyroxene, and spinel) dissolve in different proportions, therefore contributing different inputs into the composition of circulating melt.

To summarize, the Tumusun lherzolite xenoliths demonstrate the following features: (1) the formation process of mineral reaction zone is more intense toward basanite/xenolith contact, (2) the pyroxenes are not melted but dissolved in this process, (3) the influence of basanite on mineral major and trace element composition is limited to first hundreds of μm from basanite/xenolith contact, (4) the composition of Cpx3 from orthopyroxene reaction zone at basanite/xenolith contact is indicative for trace element diffusion from basanite into a melt formed via orthopyroxene dissolution, (5) the melt that circulates inside xenoliths has a composition different from that of basanite, (6) the melt circulating inside xenoliths is inhomogeneous, (7) the composition of circulating melt depends on the composition of dissolved peridotite minerals and diffusion of elements from basanite.

Experimental studies of mechanisms of orthopyroxene dissolution in silica-undersaturated alkaline melts at 1 atm and 0.4 to 2 GPa [12,13] demonstrate that SiO_2 -undersaturated melt produces incongruent dissolution of orthopyroxene to form silica- and alkali-rich melt followed by crystallization of high-magnesian olivine and clinopyroxene. The composition of the newly formed melt is determined by the composition of dissolving orthopyroxene and diffusion of elements (Ca, Al, Na, K) from basanite melt. Therefore, the secondary minerals are Mg rich as the primary minerals of peridotites.

Based on experimental studies of peridotite–melt reaction at one atmosphere [6], a two-stage model was suggested to explain the development of spongy texture around clinopyroxene and spinel in mantle xenoliths. In the first stage, orthopyroxene undergoes incongruent dissolution to produce a silica- and alkali-rich melt, and olivine. In the second stage, this newly formed melt migrates along grain boundaries and triggers incongruent dissolution of clinopyroxene and spinel [6]. As in the above experiments, the Tumusun lherzolites exhibit predominant development of clinopyroxene and spinel reaction zones in contact with orthopyroxene reaction zones and veinlets of alkali feldspar. At the same time, clinopyroxene and spinel grains also have reaction zones at basanite/xenolith contact. In the last case, it is unclear whether these reaction zones form due to interaction with basanite or before that during the reaction with a newly formed melt.

To conclude, the petrographic observations and major and trace element compositions of secondary minerals of reaction zones agree well with the two-stage model of peridotite interaction with silica-undersaturated alkaline melts [6].

5.2. Compositional Changes in Whole Rocks Due to the Basanite–Lherzolite Interaction

Marginal and central parts of three large xenoliths have similar trace element patterns, but the marginal parts demonstrate higher abundances of K_2O , LILE, and sometimes LREE-MREE (Figure 7a–c).

This difference could be caused by penetration of basanite via cracks inside the marginal parts of xenoliths, and thus, the measured composition of the marginal parts could represent a mix of lherzolite with basanite. To examine this possibility, the compositions of the lherzolite–basanite mix have been calculated for these samples according to the Formulas (1) and (2):

$$M = X * B + (1 - X) * L \quad (1)$$

$$X = \frac{(C_{K(\text{xenolith margin})} - C_{K(\text{xenolith center})})}{C_{K(\text{basanite})}} \quad (2)$$

where M is the element concentration (ppm) in lherzolite–basanite mix, B is the element concentration (ppm) in basanite, L is the element concentration (ppm) in the lherzolite xenolith center, and X is the amount of basanite (varying 0 to 1) in the mix. X was calculated by Formula (2) considering the concentration of K (potassium) in ppm (C_K) in the xenolith margin, xenolith center, and basanite.

The compositions of calculated mix are different from compositions of analyzed marginal parts of lherzolites for most trace elements, except for Dy–Yb (Figure 7a–c). In sample HD38, the calculated mix composition has an enriched trace-element pattern, while the measured composition of this xenolith center shows a depleted trace-element pattern (Figure 7a). The maxima of K on normalized diagrams cannot be obtained by the addition of a lesser amount of basanite to the marginal parts of xenoliths. Thus, the composition of the marginal parts of xenolith cannot be explained by a simple mixing of lherzolites with basanite.

To evaluate the possible gain of trace elements resulting from the lherzolite–melt interaction, the whole-rock compositions of six samples (three large and three small xenoliths) were calculated using modal composition of the samples and trace-element composition of primary olivine, clinopyroxene, and orthopyroxene acquired by LA-ICP-MS. For all samples, including centers of large xenoliths, the measured and calculated whole-rock compositions demonstrate similar (within analytical uncertainty) abundances of M-HREE, Zr, Hf, and Ti. In contrast, abundances of Rb, Ba, and often LREE are lower in the calculated compositions than in the measured ones (Figure 7). This inconsistency could be a result of both mixing with a small amount of basanite and element diffusion at contact of two melts (i.e., element diffusion from basanite into a melt formed due to orthopyroxene dissolution). The excess K, Na, Rb, and Ba and excess LREE in measured whole-rock compositions are related to the formation of feldspars and secondary clinopyroxenes, respectively. This indicates the non-isochemical interaction of lherzolites with basanite melt during the transportation of xenoliths to the surface.

6. Conclusions

1. Lherzolite xenoliths from basanites of Tumusun volcano demonstrate reaction zones in all minerals (orthopyroxene, clinopyroxene, spinel), which decrease in size from margins to the central parts of xenoliths until complete disappearance.
2. The reaction zones in minerals formed as a result of xenolith interaction with host basanite during transportation up to the surface. The mineral chemistry of the Tumusun lherzolite xenoliths agrees well with the two-stage reaction model of interaction between peridotite xenoliths and SiO₂-undersaturated alkaline basaltic melts, based on experimental data [6]. Our study implements this model by the information on trace element behavior in this process.
3. The influence of basanite melt on the major- and trace-element composition of secondary minerals of reaction zones is notable only at a distance up to 100–200 μm from the basanite/xenolith contact.
4. The major and trace element composition of secondary clinopyroxenes from orthopyroxene reaction zone at distance of ~0.3–1.0 mm from basanite/xenolith contact indicates its formation from a melt formed by dissolution of orthopyroxene and influenced by element diffusion (LILE > REE > HFSE) from the basanite melt. Farther inside xenoliths, the secondary clinopyroxenes exhibit diffusional addition of Ba.
5. During the interaction, lherzolites are enriched in K, Na, Rb, and Ba, and sometimes in La and Ce. These elements are incorporated in feldspars and pyroxenes of reaction zones, as well as in feldspar veinlets.
6. During the interaction process, the cores of reacting minerals (pyroxenes and spinel) remain homogenous and have the same major- and trace-element composition as the primary lherzolite minerals.

7. The REE patterns of primary clinopyroxene are not influenced by the interaction of lherzolites with the host basanites, but reflect the mantle stage of the lherzolite formation.

Supplementary Materials: The following supporting information can be downloaded at: <https://www.mdpi.com/article/10.3390/min13030403/s1>, Electronic Supplementary Table S1: the compositions of lherzolite minerals, calculated whole-rocks, host basanite, and reference materials.

Author Contributions: Conceptualization, M.A.G.; methodology, V.A.B. and A.A.K.; investigation, M.A.G.; data curation, A.B.P. and S.I.D.; writing—original draft preparation, M.A.G. and V.A.B.; writing—review and editing, V.A.B. and A.A.K.; visualization, A.A.K.; supervision, M.A.G.; project administration, M.A.G.; funding acquisition, M.A.G., V.A.B. and A.A.K. All authors have read and agreed to the published version of the manuscript.

Funding: The study was funded by a grant from the Russian Science Foundation № 22-27-00821, <https://rscf.ru/project/22-27-00821/> (accessed on 10 March 2023).

Data Availability Statement: The data supporting the findings of this study are available within the article and its Supplementary Materials.

Acknowledgments: The authors thank S. Simakin and E. Potapov for accurate and precise SIMS data of mineral trace element composition. I.S. Sharygin is thanked for providing access to the Raman spectrometer. The authors are grateful to E.I. Demonerova and A.V. Ivanov for supplying a sample of xenolith-bearing basanite from the Tumusun volcano. The comments of three anonymous reviewers helped to improve the paper considerably.

Conflicts of Interest: The authors declare no conflict of interest. The funders had no role in the design of the study; in the collection, analyses, or interpretation of data; in the writing of the manuscript; or in the decision to publish the results.

References

1. Bonadiman, C.; Beccaluva, L.; Coltorti, M.; Siena, F. Kimberlite-like Metasomatism and ‘Garnet Signature’ in Spinel-Peridotite Xenoliths from Sal, Cape Verde Archipelago: Relics of a Subcontinental Mantle Domain within the Atlantic Oceanic Lithosphere? *J. Petrol.* **2005**, *46*, 2465–2493. [\[CrossRef\]](#)
2. Lu, J.; Zheng, J.; Griffin, W.L.; O’Reilly, S.Y.; Pearson, N.J. Microscale Effects of Melt Infiltration into the Lithospheric Mantle: Peridotite Xenoliths from Xilong, South China. *Lithos* **2015**, *232*, 111–123. [\[CrossRef\]](#)
3. Carpenter, R.L.; Edgar, A.D.; Thibault, Y. Origin of Spongy Textures in Clinopyroxene and Spinel from Mantle Xenoliths, Hessian Depression, Germany. *Mineral. Petrol.* **2002**, *74*, 149–162. [\[CrossRef\]](#)
4. Ma, G.S.-K.; Wang, K.-L.; Malpas, J.; Iizuka, Y.; Xenophontos, C.; Turkmani, A.A.; Chan, G.H.-N.; Usuki, T.; Chan, Q.H.-S. Melt Pockets and Spongy Clinopyroxenes in Mantle Xenoliths from the Plio-Quaternary Al Ghab Volcanic Field, NW Syria: Implications for the Metasomatic Evolution of the Lithosphere. In *The Earth’s Heterogeneous Mantle*; Khan, A., Deschamps, F., Eds.; Springer International Publishing: Cham, Switzerland, 2015; pp. 205–257; ISBN 978-3-319-15626-2.
5. Su, B.-X.; Zhang, H.-F.; Sakyi, P.A.; Yang, Y.-H.; Ying, J.-F.; Tang, Y.-J.; Qin, K.-Z.; Xiao, Y.; Zhao, X.-M.; Mao, Q.; et al. The Origin of Spongy Texture in Minerals of Mantle Xenoliths from the Western Qinling, Central China. *Contrib. Mineral. Petrol.* **2011**, *161*, 465–482. [\[CrossRef\]](#)
6. Shaw, C.S.J.; Dingwell, D.B. Experimental Peridotite–Melt Reaction at One Atmosphere: A Textural and Chemical Study. *Contrib. Mineral. Petrol.* **2008**, *155*, 199–214. [\[CrossRef\]](#)
7. Chattopadhyaya, S.; Ghosh, B.; Morishita, T.; Nandy, S.; Tamura, A.; Bandyopadhyay, D. Reaction Microtextures in Entrapped Xenoliths in Alkali Basalts from the Deccan Large Igneous Province, India: Implications to the Origin and Evolution. *J. Asian Earth Sci.* **2017**, *138*, 291–305. [\[CrossRef\]](#)
8. Pan, S.; Zheng, J.; Yin, Z.; Griffin, W.L.; Xia, M.; Lin, A.; Zhang, H. Spongy Texture in Mantle Clinopyroxene Records decompression-Induced Melting. *Lithos* **2018**, *320–321*, 144–154. [\[CrossRef\]](#)
9. Ashchepkov, I.V. *Deep-Seated Xenoliths of the Baikal Rift*; Nauka: Novosibirsk, Russia, 1991.
10. Ionov, D.A.; O’Reilly, S.Y.; Ashchepkov, I.V. Feldspar-Bearing Lherzolite Xenoliths in Alkali Basalts from Hamar-Daban, Southern Baikal Region, Russia. *Contrib. Mineral. Petrol.* **1995**, *122*, 174–190. [\[CrossRef\]](#)
11. Arai, S.; Abe, N. Reaction of Orthopyroxene in Peridotite Xenoliths with Alkali-Basalt Melt and Its Implication for Genesis of Alpine-Type Chromitite. *Am. Mineral.* **1995**, *80*, 1041–1047. [\[CrossRef\]](#)
12. Shaw, C.S.J. Dissolution of Orthopyroxene in Basanitic Magma between 0.4 and 2 GPa: Further Implications for the Origin of Si-Rich Alkaline Glass Inclusions in Mantle Xenoliths. *Contrib. Mineral. Petrol.* **1999**, *135*, 114–132. [\[CrossRef\]](#)

13. Shaw, C.S.J.; Thibault, Y.; Edgar, A.D.; Lloyd, F.E. Mechanisms of Orthopyroxene Dissolution in Silica-Undersaturated Melts at 1 Atmosphere and Implications for the Origin of Silica-Rich Glass in Mantle Xenoliths. *Contrib. Mineral. Petrol.* **1998**, *132*, 354–370. [[CrossRef](#)]
14. García Serrano, J.; Villaseca, C.; Pérez-Soba, C. Depleted Lherzolite Xenoliths from the Leucititic Morrón de Villamayor Volcano (Calatrava Volcanic Field, Spain). *Lithos* **2021**, *380–381*, 105830. [[CrossRef](#)]
15. Yarmolyuk, V.V.; Kovalenko, V.I.; Ivanov, V.G.; Pokrovskii, B.G. Magmatism and Geodynamics of the Southern Baikal Volcanic Region (Mantle Hot Spot): Results of Geochronological, Geochemical, and Isotopic (Sr, Nd, and O) Investigations. *Petrology* **2003**, *11*, 1–30.
16. Yarmolyuk, V.V.; Kovalenko, V.I.; Ivanov, V.G. Intraplate Late Mesozoic-Cenozoic volcanic province of Central-East Asia—Projection of the hot mantle field. *Geotektonika* **1995**, *29*, 41–67.
17. Ivanov, A.V.; Demonerova, E.I.; He, H.; Perepelov, A.B.; Travin, A.V.; Lebedev, V.A. Volcanism in the Baikal Rift: 40 years of Active-versus-Passive Model Discussion. *Earth-Sci. Rev.* **2015**, *148*, 18–43. [[CrossRef](#)]
18. Makrygina, V.A.; Belichenko, V.G.; Reznitsky, L.Z. Types of Paleoisland Arcs and Back-Arc Basins in the Northeast of the Paleasian Ocean (from Geochemical Data). *Russ. Geol. Geophys.* **2007**, *48*, 107–119. [[CrossRef](#)]
19. Kovach, V.; Salnikova, E.; Wang, K.-L.; Jahn, B.-M.; Chiu, H.-Y.; Reznitskiy, L.; Kotov, A.; Iizuka, Y.; Chung, S.-L. Zircon Ages and Hf Isotopic Constraints on Sources of Clastic Metasediments of the Slyudyansky High-Grade Complex, Southeastern Siberia: Implication for Continental Growth and Evolution of the Central Asian Orogenic Belt. *J. Asian Earth Sci.* **2013**, *62*, 18–36. [[CrossRef](#)]
20. Kotov, A.B.; Salnikova, E.B.; Reznitsky, L.Z.; Vasil'ev, E.P.; Kozakov, I.K.; Yakovleva, S.Z.; Kovach, V.P.; Berezhnaya, N.G. Age of Metamorphism of the Slyudyanka Crystalline Complex, Southern Baikal Area: U–Pb Geochronology of Granitoids. *Petrology* **1997**, *5*, 338–349.
21. Litasov, K.; Taniguchi, H. *Mantle Evolution Beneath the Baikal Rift*; CNEAS Monograph Series; Tōhoku Ajia Kenkyū Sentā Sōsho; dai 5-gō; Center for Northeast Asian Studies, Tohoku University: Sendai-shi, Japan, 2002; ISBN 978-4-901449-04-5.
22. Litasov, K.D.; Litasov, Y.D.; Malkovets, V.G. Metasomatism and Transformations of the Upper Mantle beneath the Southern Baikal Territory: Evidence from Xenoliths of the Bartoy Volcanic Area. *Geochem. Int.* **2005**, *43*, 242–267.
23. Tsypukova, S.S.; Perepelov, A.B.; Demonerova, E.I.; Pavlova, L.A.; Travin, A.V.; Puzankov, M.Y. Origin and Evolution of Neogene Alkali-Basaltic Magmas in the Southwestern Flank of the Baikal Rift System (Heven Lava Plateau, Northern Mongolia). *Russ. Geol. Geophys.* **2014**, *55*, 190–215. [[CrossRef](#)]
24. Woodhead, J.D.; Hellstrom, J.; Hergt, J.M.; Greig, A.; Maas, R. Isotopic and Elemental Imaging of Geological Materials by Laser Ablation Inductively Coupled Plasma-Mass Spectrometry. *Geostand. Geoanalyt. Res.* **2007**, *31*, 331–343. [[CrossRef](#)]
25. Paton, C.; Hellstrom, J.; Paul, B.; Woodhead, J.; Hergt, J. Lolite: Freeware for the Visualisation and Processing of Mass Spectrometric Data. *J. Anal. At. Spectrom.* **2011**, *26*, 2508–2518. [[CrossRef](#)]
26. Bottazzi, P.; Ottolini, L.; Vanucci, R.; Zanetti, A. An Accurate Procedure for the Quantification of Rare Earth Elements in Silicates. In Proceedings of the Secondary Ion Mass Spectrometry, New Orleans, LA, USA, 31 July–5 August 1994; Wiley: Yokohama, Japan, 1994; pp. 927–930.
27. Amosova, A.A.; Panteeva, S.V.; Tatarinov, V.V.; Chubarov, V.M.; Finkelstein, A.L. X-ray Fluorescence Determination of Major Rock Forming Elements in Small Samples 50 and 110 Mg. *Anal. Control* **2015**, *19*, 130–138.
28. Wang, Y.; Han, B.; Griffin, W.L.; Zhang, L.; Shu, G. Post-Entrainment Mineral-Magma Interaction in Mantle Xenoliths from Inner Mongolia, Western North China Craton. *J. Earth Sci.* **2012**, *23*, 54–76. [[CrossRef](#)]
29. Morimoto, N. Nomenclature of Pyroxenes. *Mineral. Petrol.* **1988**, *39*, 55–76. [[CrossRef](#)]
30. Matson, D.W.; Sharma, S.K.; Philipots, J.A. Raman Spectra of Some Tectosilicates and of Glasses along the Orthoclase-Anorthite and Nepheline-Anorthite Joins. *Am. Mineral.* **1986**, *71*, 694–704.
31. McDonough, W.F.; Sun, S.-S. The Composition of the Earth. *Chem. Geol.* **1995**, *120*, 223–253. [[CrossRef](#)]
32. Bonadiman, C.; Coltorti, M.; Beccaluva, L.; Griffin, W.L.; O'Reilly, S.Y.; Siena, F. Metasomatism versus Host Magma Infiltration: A Case Study of Sal Mantle Xenoliths, Cape Verde Archipelago. In *Volcanism and Evolution of the African Lithosphere*; Geological Society of America: Boulder, CO, USA, 2011; ISBN 978-0-8137-2478-2.
33. Foley, S.F.; Andronikov, A.V.; Jacob, D.E.; Melzer, S. Evidence from Antarctic Mantle Peridotite Xenoliths for Changes in Mineralogy, Geochemistry and Geothermal Gradients beneath a Developing Rift. *Geochim. Et Cosmochim. Acta* **2006**, *70*, 3096–3120. [[CrossRef](#)]
34. Foley, S.F.; Andronikov, A.V.; Halpin, J.A.; Daczko, N.R.; Jacob, D.E. Mantle Rocks in East Antarctica. *Memoirs* **2023**, *56*, 17–32. [[CrossRef](#)]
35. Miller, C.; Zanetti, A.; Thöni, M.; Konzett, J.; Klötzli, U. Mafic and Silica-Rich Glasses in Mantle Xenoliths from Wau-En-Namus, Libya: Textural and Geochemical Evidence for Peridotite–Melt Reactions. *Lithos* **2012**, *128–131*, 11–26. [[CrossRef](#)]
36. Litasov, K.D.; Litasov, Y.D.; Mekhonoshin, A.S.; Malkovets, V.G. Mineralogy of Mantle Xenoliths from Pliocene Basanites of the Dzhilinda River (Vitim Volcanic Field). *Russ. Geol. Geophys.* **2000**, *41*, 1534–1556.
37. Chen, P.; Fang, N.; Yuan, X. Geochemical Insights from Clinopyroxene Phenocrysts into the Magma Evolution of an Alkaline Magmatic System from the Sanshui Basin, South China. *Minerals* **2021**, *11*, 1295. [[CrossRef](#)]

38. Vannucci, R.; Bottazzi, P.; Wulff-Pedersen, E.; Neumann, E.-R. Partitioning of REE, Y, Sr, Zr and Ti between Clinopyroxene and Silicate Melts in the Mantle under La Palma (Canary Islands): Implications for the Nature of the Metasomatic Agents. *Earth Planet. Sci. Lett.* **1998**, *158*, 39–51. [[CrossRef](#)]
39. Beard, C.D.; van Hinsberg, V.J.; Stix, J.; Wilke, M. Clinopyroxene/Melt Trace Element Partitioning in Sodic Alkaline Magmas. *J. Petrol.* **2019**, *60*, 1797–1823. [[CrossRef](#)]
40. Holycross, M.E.; Bruce Watson, E. Diffusive Fractionation of Trace Elements in Basaltic Melt. *Contrib Miner. Pet.* **2016**, *171*, 80. [[CrossRef](#)]
41. Behrens, H.; Hahn, M. Trace Element Diffusion and Viscous Flow in Potassium-Rich Trachytic and Phonolitic Melts. *Chem. Geol.* **2009**, *259*, 63–77. [[CrossRef](#)]

Disclaimer/Publisher’s Note: The statements, opinions and data contained in all publications are solely those of the individual author(s) and contributor(s) and not of MDPI and/or the editor(s). MDPI and/or the editor(s) disclaim responsibility for any injury to people or property resulting from any ideas, methods, instructions or products referred to in the content.